DOI: 10.1002/ ((please add manuscript number))

Article type: Full Paper

Degenerately hydrogen doped molybdenum oxide nanodisks for ultra-sensitive plasmonic biosensing

Bao Yue Zhang, Ali Zavabeti, Adam F. Chrimes, Farjana Haque, Luke A. O'Dell, Hareem Khan, Nitu Syed, Robi Datta, Yichao Wang, Anthony S. R. Chesman, Torben Daeneke, Kourosh Kalantar-zadeh, Jian Zhen Ou**

B. Y. Zhang, A. Zavabeti, Dr. A. F. Chrimes, F. Haque, H. Khan, N. Syed, R. Datta, Dr. T. Daeneke, Prof. K. Kalantar-zadeh, Dr. J. Z. Ou

School of Engineering, RMIT University, Melbourne, VIC 3000, Australia

E-mail: jianzhen.ou@rmit.edu.au and kourosh.kalantar@rmit.edu.au

Dr. A. F. Chrimes

Department of Chemistry and Applied Biosciences, Institute for Chemical and Bioengineering, ETH Zürich, Zürich 8093, Switzerland

Dr. L. A. O'Dell

Institute for Frontier Materials, Deakin University, Geelong, Victoria 3216, Australia

Dr. Y. Wang

School of Life and Environmental Sciences, Deakin University, Geelong, Victoria 3216, Australia

Dr. A. S. R. Chesman

CSIRO Manufacturing, Ian Wark Laboratories, Clayton, Victoria 3168, Australia

Keywords: tunable plasmonics, two-dimensional, sensors, atomically thin, intercalation, transition metal oxide

Plasmonic biosensors based on noble metals generally suffer from low sensitivities if the perturbation of refractive-index in the ambient is not significant. In contrast, the features of degenerately doped semiconductors offer new dimensions for plasmonic biosensing, by allowing charge based detection. Here we demonstrate this concept in plasmonic hydrogen doped molybdenum oxides (H_xMoO_3), with the morphology of two-dimensional nanodisks, using a representative enzymatic glucose sensing model. Based on the ultra-high capacity of the molybdenum oxide nanodisks for accommodating H^+, the plasmon resonance wavelengths of H_xMoO_3 are shifted into visible-near infrared wavelengths. These plasmonic features alter significantly as a function of the intercalated H^+ concentration. The facile H^+ de-intercalation out of H_xMoO_3 provides an exceptional sensitivity and fast kinetics to charge perturbations during enzymatic oxidation. The optimum sensing response is found at $H_{1.55}MoO_3$, achieving a detection limit of 2 nM at 410 nm, even when the biosensing platform is adapted into an LED-photodetector setup. The performance is superior in comparison to all previously reported plasmonic enzymatic glucose sensors, providing a great opportunity in developing high performance biosensors.

1. Introduction

Degenerately doped semiconductors are an emerging class of plasmonic materials for which plasmonic features can be controlled by the concentration of dopants in the crystal structure.[1] In contrast, owing to the relatively small free charge carrier concentrations compared to traditional plasmonic noble metals, perturbations of charge carrier density in doped semiconductors affects the plasmonic spectral position.[2] This unique characteristic is particularly useful for applying this category of plasmonic crystals in probing charge transfer during biochemical processes, allowing for the development of charge-sensitive biosensors.[3] The corresponding biosensing mechanism is hence different from that of conventional noble metal based plasmonic biosensors which are mostly refractive-index mediated.[3c]

The main category of plasmonic degenerately doped semiconductors is comprised of doped oxides with embedded non-migrating dopants.[1a, 1c, 1d, 4] Due to the intrinsic crystal structure of these materials, their ability to accommodate dopants is rather limited resulting in free charge carrier concentrations of less than 10^{21} cm^{-3}. This causes the plasmonic absorption band being located within the mid-infrared (MIR) and short-wavelength infrared (SWIR) regions,[1a, 1c, 1d, 4] which are not easily accessed in standard optical systems.

Sub-stoichiometric metallic compounds, such as copper chalcogenides, and tungsten and molybdenum oxides, are a sub-class of degenerately doped semiconductors that have plasmonic features tuned to the more commercially viable near infrared (NIR) or near-red end of the visible spectrum.[5] However, the relatively high stability of these vacancies may not facilitate the charge

exchange during biochemical events, rendering these plasmonic systems less sensitive and slow kinetics for biosensing.[3b, 5d, 6]

The key to advancing the concept of degenerately doped materials for plasmonic biosensing is to find suitable crystals which can operate in the visible light to NIR region, while maintaining ultra-high sensitivity and fast kinetics. This implies two prerequisites: (1) the dopant concentration should be large enough to generate free charge carrier concentrations > 10^{22} cm^{-3}; and (2) dopants and concurrently injected free electrons are easily exchanged from the host structure during biochemical events. To fulfil these criteria, we examine hydrogen infused structures that can be reversibly doped with small ions, concurrently carrying the free charge carriers with themselves into and out of the plasmonic system. This alteration in charge rapidly changes the plasmon resonance features, hence creating a sensitive platform. H^+, as the smallest ion in nature, is a suitable dopant due to its strong ability to fast migrate and enter/exist within interstitial sites of inorganic compounds, especially those with van der Waals gaps, while avoiding large structural expansion and significant alteration of the host crystal structure.[7]

Orthorhombic molybdenum trioxide (MoO_3) has a unique layered structure that is a suitable host for accommodating a large number of H^+, and the theoretical H^+/MoO_3 ratio can be as high as 2:1.[8] The intercalated H^+ ions normally reside either in the van der Waals gaps between double layers of MoO_6 octahedra in the MoO_3 crystal structure or on the intralayer sites on the zigzaging chains along the channels,[9] giving an intercalated compound called “hydrogen molybdenum bronze (H_xMoO_3)”.[8] Simultaneously, the intercalated H^+ ions within the van der Waals gaps contribute to the exfoliation of the layered MoO_3, resulting in two-dimensional (2D) morphologies of the intercalated crystals which also facilitate biosensing application due to the large surface area.[5d, 6a] Depending on the

intercalated H^+ concentration, there are three thermodynamically stable phases which can be identified for H_xMoO_3, including type 1 ($0.23 < x < 0.40$) (**Figure 1**a), 2 ($0.85 < x < 1.04$) (Figure 1b) and 3 ($1.55 < x < 1.72$) (Figure 1c).[8] In type 1 H_xMoO_3, the H^+ intercalation is topotactic and the orthorhombic crystal phase is maintained. However, as the amount of intercalated H^+ increases, type 2 and 3 H_xMoO_3 show a phase transformation from orthorhombic into monoclinic crystal structures.[9a, 9b, 10] A stoichiometric phase 4 ($x = 2$) with the maximum intercalated H^+ content also exists but is highly unstable.[11] Doping also affects the electronic structure with the intercalation of H^+ in MoO_3, leading to the reduction of the Mo oxidation states and eventually the formation of low-dimensional quasi-metals due to the partially filled Mo *4d* orbitals.[5d] The concurrently injected electrons during the synthesis of H_xMoO_3 are mostly delocalised, which is different from other layered oxides such as V_2O_5.[7b] Therefore, the resulting free electron concentration in H_xMoO_3 can be as high as ~10^{22} cm^{-3}, which is sufficient to generate a plasmon resonance in the visible light range.[7b] More importantly, the surface of H_xMoO_3 is highly reducible,[12] which implies a strong reactivity of the intercalated H^+ towards surrounding chemicals with an appropriate redox potential. Such advantages lead to the assumption that the plasmonics of degenerately doped H_xMoO_3, particularly at large *x* values, should offer extraordinary sensitivities. However, this concept is yet to be proven.

In this work, we explore the application of 2D H_xMoO_3 atomically thin disks, which have wide plasmonic tunability across the visible and NIR region, to the ultra-sensitive and rapid detection of biochemicals. A typical biological redox event based on an enzymatic glucose sensing model is used. Here the biological redox event occurs locally in the 2D H_xMoO_3 plasmonic structure, causing a rapid change in the H^+ dopant levels and hence modulates free electron concentrations, resulting in large

perturbations of the plasmonic properties. We show that the unique, widely-tunable window of the H^+-driven plasmonic spectrum offers the possibility of optimising the doping levels for ultra-sensitive biosensing. This plasmonic sensing platform is then integrated into a hand-held light-emitting diode (LED)-photodetector setup that proves a practical implementation of the concept at such extraordinary sensitivities.

2. Results and Discussion

The facile and controlled synthesis of plasmonic H_xMoO_3 is one of the most important criteria to realising the biosensing platform. The conventional synthesis of H_xMoO_3 is mainly *via* the reduction intercalation of MoO_3 using a Zn/HCl aqueous solution, or the spill-over approach using noble-metal coated MoO_3 in the presence of H_2 gas.[7b, 8, 9b] However, these methods are not suitable for biosensing applications as: (1) the nano-sized metal residing on the surface of H_xMoO_3 will have an unknown effect on the surrounding biomolecules; and (2) the H^+ doping is not homogenous across the nanostructure and hence the H_xMoO_3 phase cannot be finely controlled.[7, 13] Here, a large scalable hydrothermal synthesis method is demonstrated.

Ammonium molybdate tetrahydrate ($(NH_4)_6Mo_7O_{24}{\cdot}4H_2O$) is a well-known precursor for forming MoO_3 using hydrothermal synthetic methods.[14] In our case, tartaric acid ($C_4H_6O_6$) is added to the precursor solution as a H^+ source for intercalation, similar to other reducing agents.[15] Hydrogen doping has been used as a common connotation when H is inserted into α-MoO_3, producing absorbed protons and lending the injected electrons to the layers.[5d, 7a] The H atom can be located at the terminal and/or asymmetric oxygen. When H is absorbed and concurrently electrons are

injected, the free electron concentration increases by many orders of magnitude, depending on the number of H intercalated per unit cell. The location of the H within the unit cell depends on the *x* value in H_xMoO_3. The level of H^+ dopants is proposed to be readily controlled by altering the pH value of the precursor solution, as the pH value has been recognized to greatly influence the speciation of molybdate ions in the aqueous solution. When the pH value is between 2 and 3, the molybdate species in aqueous solutions are dominated by H_2MoO_4 and $Mo(OH)_6$.[16] When the pH value falls below 2, the $[H_3MoO_4]^+$ and $[Mo(OH)_5(H_2O)]^+$ ions start to appear in the solution,[16] which is hypothesized to prohibit the H^+ intercalation into MoO_3.

To verify this hypothesis, solid state ^1H magic-angle spinning (MAS) nuclear magnetic resonance (NMR) spectroscopy is used to confirm the H^+ intercalation into the host MoO_3 structure during the hydrothermal process. Four samples, synthesized at different pH values of 1, 1.5, 2 and 2.5, are investigated. After the hydrothermal reaction, the pH values of the pH 1.5, 2 and 2.5 samples are increased to ~2, ~4 and ~5, respectively, while the pH 1 sample remains constant. Such increases of pH values confirm that tartaric acid is decomposed during the hydrothermal reaction and acts as the H^+ source for intercalating in MoO_3. From Figure 1d, there is no distinguishable peak found in the pH 1 sample, indicating that no H^+ intercalation has occurred even in the presence of the tartaric acid, confirming $[H_3MoO_4]^+$ and $[Mo(OH)_5(H_2O)]^+$ ions are not favorable to the accommodation of the intercalated H^+ ions at this pH. When the pH is increased to 1.5 during the synthesis, peaks appear at 2.6, 3.2 and 4.2 ppm, which can all be ascribed to the presence of Mo-OH groups bonded mainly with asymmetric oxygen (corner-sharing oxygen) and terminal oxygen atoms (unshared oxygen atom).[9a, 17] For the pH 2 sample, the intensity of the 3.2 ppm peak decreases and becomes a broad shoulder, possibly ascribed that part of the intercalated H^+ ions shifts the bonding locations between

asymmetric oxygen and terminal oxygen atoms (Figure 1a and b).[9a] In the case of the pH 2.5 sample, the 2.6 ppm peak is broadened and the 4.2 ppm peak becomes dominant. It is suggested that the favorable location for large amount of intercalated H^+ into MoO_3 is predominantly at the terminal oxygen atom sites (Figure 1c).[9, 13, 18] Therefore, we can associate the emergence of peaks at 2.6 and 3.2 ppm to H^+ bonded to the asymmetric coordinated oxygen atoms, while the 4.2 ppm peak is attributed to H^+ bonded with the terminal oxygen atoms. For the samples obtained at pH 1.5, 2 and 2.5, a small hump can be observed in the region between 0.5 and 1 ppm, which can be ascribed to surface adsorbed water molecules that possibly originate from the ambient environment.[17]

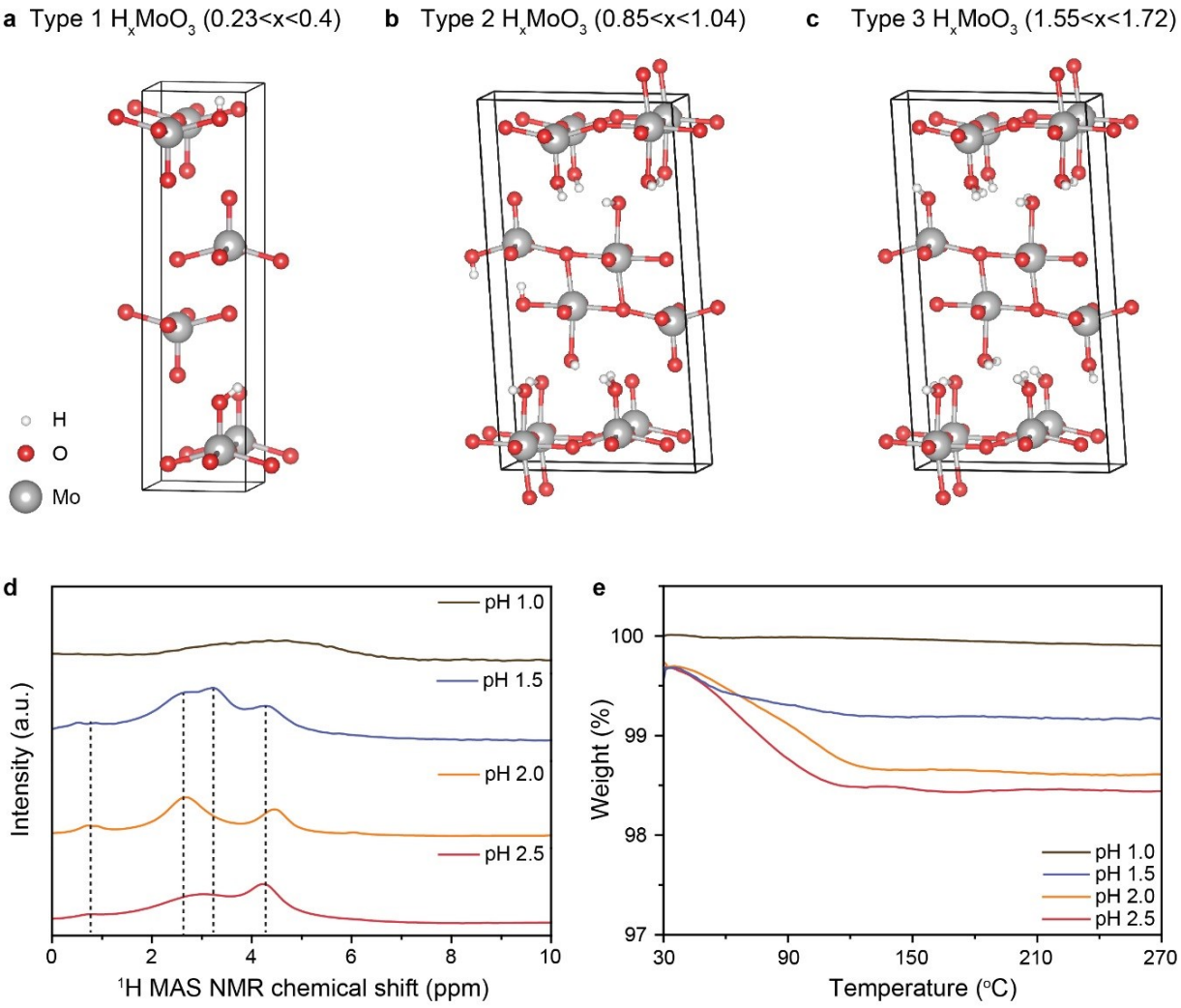

Figure 1. Overview of the crystal structures of (a) type 1 H_xMoO_3 showing OH groups located at both asymmetric and terminal oxygen atoms,[9a, 12] (b) type 2 H_xMoO_3 showing OH and OH_2 groups mainly located at terminal oxygen atoms,[9a, 9c] and (c) type 3 H_xMoO_3 showing OH and OH_2 groups predominantly located at terminal oxygen atoms.[9a, 9c] (d) ^{1}H MAS NMR spectra of samples hydrothermally synthesized at pH 1, 1.5, 2 and 2.5. (e) The corresponding TGA patterns of samples hydrothermally synthesized at pH 1, 1.5, 2 and 2.5 at temperatures between 30 and 270°C in an N_2 gas environment.

In order to further verify the hypothesis and determine the amount of intercalated H^+ presented in the MoO_3, thermogravimetric analysis (TGA) is performed on the afore-mentioned samples in an N_2 gas environment. From Figure 1e, there is almost no observable change of weight for the pH 1 sample up to 270°C. This is expected as the NMR result confirms no H^+ intercalation occurred at this pH level. For the pH 1.5 sample, an initial weight loss of ~0.27% is seen at temperatures between ~40 and 60°C. Subsequently, there is a further weight loss of ~0.25% in the region from ~60 to 160°C, which corresponds well to the decomposition pattern of type 1 H_xMoO_3 reported in the literature.[8] It is also believed that the initial drop is due to the evaporation of surface adsorbed water molecules on the sample as the corresponding temperature range is too low for the decomposition of H_xMoO_3 when the amount of intercalated H^+ is small.[8, 19] In comparison, such initial weight losses are not obvious for both pH 2 and 2.5 samples, possibly being convoluted with the weight loss steps corresponding to the decomposition of H_xMoO_3. By comparing the weight differences at 60 and 160°C, the losses related to the release of H^+ are 0.79% and 1.01% for pH 2 and 2.5 samples, respectively. Due to the fact that the release of intercalated H^+ from MoO_3 at elevated temperatures is mainly in the form of H_2,[8] by comparing with the theoretical calculation shown in the **Table S1**, the pH 1.5 sample can be identified as $H_{0.3}MoO_3$, which belongs to type 1 H_xMoO_3 (Figure 1a), while the pH 2 and pH 2.5 samples are characterised as $H_{0.91}MoO_3$ (type 2 H_xMoO_3 – Figure 1b) and $H_{1.55}MoO_3$ (type 3 H_xMoO_3 – Figure 1c), respectively.[8]

The TGA graph along with higher temperature is shown in **Figure S1**. When the temperature is above 160°C, the TGA curves of all samples have two obvious drops starting at ~280-320°C and ~430-460°C. The first drop can be ascribed to the loss of water in the crystal structure,[20] while the second one indicates the formation of oxygen vacancy.[21] The morphological characterization of the samples is carried out using atomic force microscopy (AFM). The MoO_3 sample, which was obtained at a pH of 1, is composed of belt shape structures with sharp tips (**Figure 2**a) with an average thickness mainly in the range between 30 to 50 nm (**Figure S2**). Interestingly, the morphologies of all H_xMoO_3 samples are starkly different from that of MoO_3 nanobelts synthesized at lower pH values. It seems that at the higher pH values the belts are broken into individual small disks, possibly due to the rapid H^+ intercalation during the hydrothermal synthesis.[5d] Figure 2b–d show representative AFM images for $H_{0.3}MoO_3$, $H_{0.91}MoO_3$ and $H_{1.55}MoO_3$, respectively. They are all confirmed to adopt planar 2D disk-like morphologies. Interestingly, the thickness is decreased from ~6.6 (equivalent to 5 unit cell thickness for α-MoO_3[22]) to ~1.5 nm (equivalent to 1 unit cell thickness for α-MoO_3[22]) as the intercalated H^+ amount is increased, while their lateral dimensions are not changed significantly. This trend is also confirmed by the peak locations of both thickness and lateral dimension distribution frequencies for each type of H_xMoO_3 based on the assessment of AFM images from a large number of samples (**Figure S3**), revealing the contribution of H^+ intercalation to the exfoliation of layered MoO_3.[5d] The scanning electron microscope (SEM) image of H_xMoO_3 is shown in **Figure S4**, and **Figure S5** shows more collective AFM images of α-MoO_3 and each type of H_xMoO_3.

Low and high resolution transmission electron miscopy (TEM) are used to confirm the dimensions and reveal the crystal structures of both stoichiometric and H_xMoO_3 samples. The inset TEM image in Figure 2e confirms the belt shape nature of MoO_3 with sharp ends. The high resolution TEM

(HRTEM) image in Figure 2e demonstrates a crystalline structure with a lattice spacing of 0.39 nm, which is ascribed to the (100) plane of α-MoO_3.[5d] The corresponding selective area electron diffraction (SAED) pattern is presented in the **Figure S6**a. with clearly distinguishable diffraction spots representing the (101) and (110) planes of orthorhombic α-MoO_3.[23] The morphologies of all three types of H_xMoO_3 are confirmed to be 2D nanodisks with average dimensions of less than 50 nm (insets of Figure 2f–h). For $H_{0.3}MoO_3$ (Figure 2f), the crystal lattice is polycrystalline with smaller crystalline domains (white dotted area), which is also confirmed by the corresponding SEAD pattern showing a ring structure in addition to the presence of the (101) plane of α-MoO_3 (Figure S6b). In the cases of $H_{0.91}MoO_3$ and $H_{1.55}MoO_3$, the crystal structures are completely disordered (Figure 2g and h and Figure S6c and d), which is a typical observation for a high degree of ion intercalation.[5d, 24]

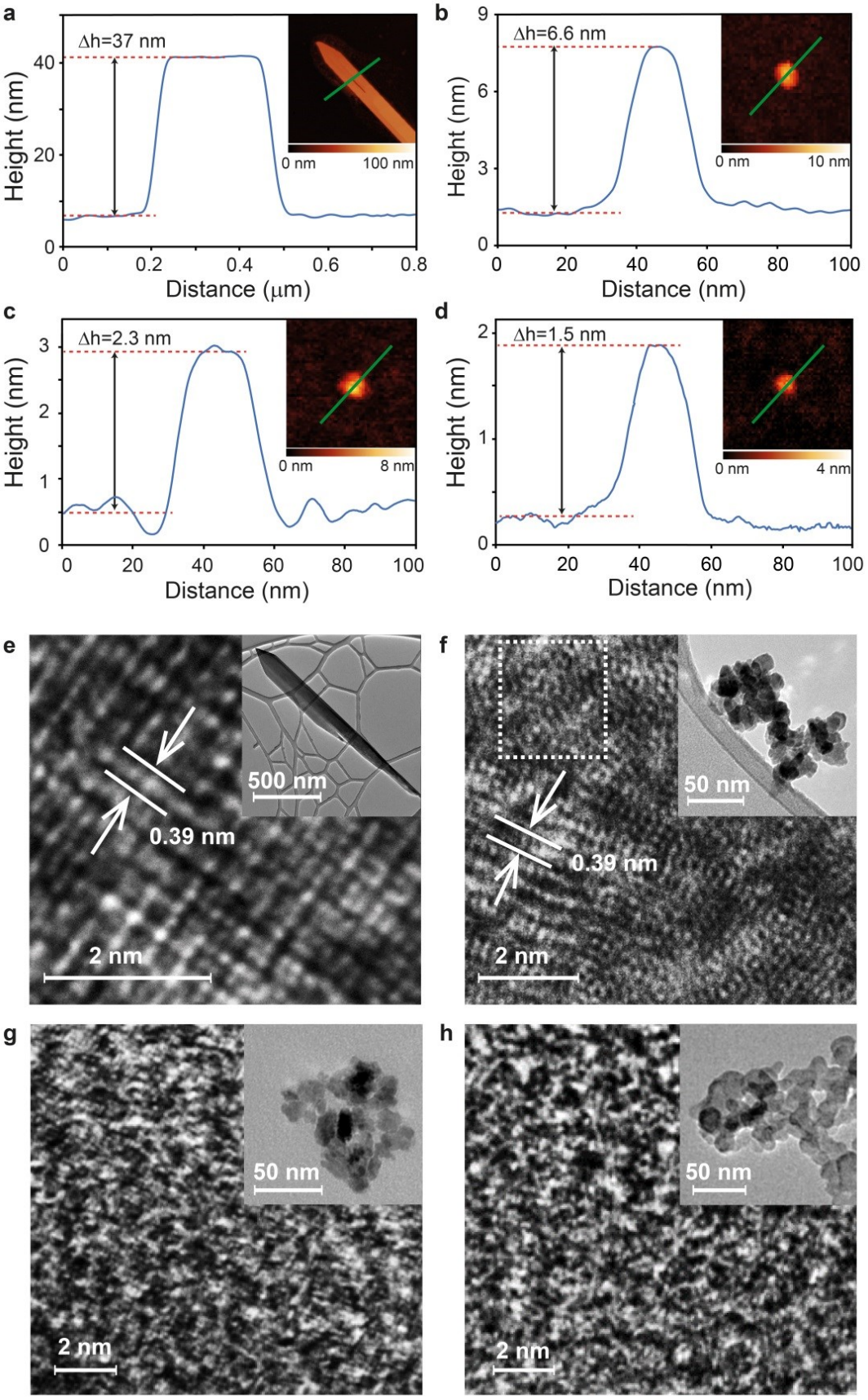
a
Δh=37 nm
Height (nm)
Distance (μm)
0 nm
100 nm
b
Δh=6.6 nm
Height (nm)
Distance (nm)
0 nm
10 nm
c
Δh=2.3 nm
Height (nm)
Distance (nm)
0 nm
8 nm
d
Δh=1.5 nm
Height (nm)
Distance (nm)
0 nm
4 nm
e
500 nm
0.39 nm
2 nm
f
50 nm
0.39 nm
2 nm
g
50 nm
2 nm
h
50 nm
2 nm

Figure 2. AFM images of (a) MoO_3 obtained at pH 1, (b) $H_{0.3}MoO_3$ obtained at pH 1.5, (c) $H_{0.91}MoO_3$ obtained at pH 2 and (d) $H_{1.55}MoO_3$ obtained at pH 2.5. HRTEM images of (e) MoO_3, (f) $H_{0.3}MoO_3$, (g) $H_{0.91}MoO_3$ and (h) $H_{1.55}MoO_3$. Insets are the corresponding low resolution TEM images.

X-ray diffraction (XRD) measurements are also utilised to assess the crystal structure (**Figure 3**a). For the MoO_3 sample, the dominant peaks at 12.7, 25.7 and 38.92° correspond to the (020), (040) and (060) crystal planes of α-MoO_3 (JCPDS card no: 05-0508).[13, 25] As suggested in the literature, MoO_3 with a 2D configuration has a strong planar nature which results in the domination of (0*k*0) (*k* = 2, 4 and 6 etc.). Additionally, after the drop casting, which is used for preparation of samples for XRD, these planar sheets mostly stack up in parallel to the substrate.[26] In such cases, other peaks such as (110) and (021) are of very low intensity or even do not emerge in XRD profiles.[22, 27] For $H_{0.3}MoO_3$, portions of the afore-mentioned peaks are slightly shifted toward smaller values and their intensities are greatly reduced, which is caused by the emergence of polycrystallinity. According to the Bragg Formula, a smaller 2Θ value means a larger interplane distance. Therefore, such peak shifts indicate that the intercalated H^+ ions, bonded with the terminal oxygen atoms, enlarge the interlayer spacings.[7a] As expected, no XRD peaks can be measured for the $H_{0.91}MoO_3$ and $H_{1.55}MoO_3$ samples, confirming their complete transformation to disordered structures upon high levels of H^+ intercalation.

The Raman spectra of MoO_3 and the three types of H_xMoO_3 samples are also obtained to investigate the influence of H^+ intercalation on the crystal structure and chemical bonding. For the MoO_3 sample, strong peaks appear at 246, 284, 292, 338, 379, 667, 818 and 995 cm^{-1}, all ascribed to the

orthorhombic α-MoO_3 structure (peak assignment in **Supporting Information Note S1**). From Figure 3b, the structural distortion of $H_{0.3}MoO_3$ upon H^+ intercalation results in a decrease of intensity and a significant broadening of MoO_3 Raman peak signatures.[7a, 28] New peaks appear at 458, 489 and 740 cm^{-1}, which can be assigned to the symmetric coordinated oxygen (Mo−O) stretching vibration, the Mo=O stretching mode, and the asymmetric coordinated oxygen atom (Mo−O) stretching vibration of H_xMoO_3, respectively.[5d, 13, 28a] For $H_{0.91}MoO_3$, the peaks at 818 and 995 cm^{-1} are not present. Instead, broad peaks appear at 860 and 950 cm^{-1} which are both characteristic of Mo−OH, suggesting the significant formation of hydroxyl groups in $H_{0.91}MoO_3$.[29] In the case of $H_{1.55}MoO_3$, the Raman spectrum is similar to $H_{0.91}MoO_3$ with further enhancement of the peak intensity at 740 cm^{-1}, suggesting an increase in the amount of intercalated H^+ ions in the host structure.

X-ray photoelectron spectroscopy (XPS) is used to confirm the stoichiometry of the samples as shown in Figure 3c. The doublet at 236.0 and 232.9 eV are attributed to 3d 3/2 and the 3d 5/2 orbital electrons of Mo^{6+}, respectively. The energy gap between them is 3.1 eV and the integral areas between the two doublets have a 2:3 ratio, both of which are in agreement with previous characterization of α-MoO_3.[5d, 30] In all three types of H_xMoO_3 samples, the intercalated H^+ and the concurrently injected electron result in the appearance of Mo^{5+} and Mo^{4+} oxidation states.[5d, 31] The peaks appearing at 231.5 and 234.8 eV can be assigned to the Mo^{5+} oxidation peak, while the Mo^{4+} oxidation peaks are observed at 229.9 and 232.9 eV. For the slightly intercalated $H_{0.3}MoO_3$, the signature of Mo^{6+} is dominated by a small amount of Mo^{5+} and Mo^{4+}. The Mo^{6+}: Mo^{5+}: Mo^{4+} ratio is calculated to be 68:21:11. The amounts of Mo^{5+} and Mo^{4+} are significantly increased in the moderately intercalated $H_{0.91}MoO_3$ with a smaller Mo^{6+}: Mo^{5+}: Mo^{4+} ratio of 29:39:32. For the highly intercalated $H_{1.55}MoO_3$, the signature of Mo^{6+} almost disappears, and instead, Mo predominately

adopts a 5+ and 4+ oxidation states in the sample with the ratio between Mo^{6+}, Mo^{5+} and Mo^{4+} being 6:53:41.

Figure 3d shows the O1s XPS spectra of the samples, which allows for the investigation of the interaction between the intercalated H^+ and the structural oxygen atoms. For MoO_3, the peak at 530.48 eV can be attributed to an Mo−O group.[32] A tiny peak appearing at 531.6 eV indicates the formation of Mo−OH bonding.[32] As the NMR results indicate that no H^+ intercalation occurred within this crystal structure, this OH group can be ascribed to surface adsorbed water from the ambient environment. For all types of H_xMoO_3 samples, it is found that the peak for the OH group increases in intensity with higher amount of intercalated H^+. In addition, a small peak appeared at 532.98 eV, indicating the formation of OH_2 groups for both $H_{0.91}MoO_3$ and $H_{1.55}MoO_3$. The phenomenon is consistent with the literature, in which large amount of H^+ intercalation leads to the formation of OH_2 groups in the terminal oxygen atoms.[9a, 9b]

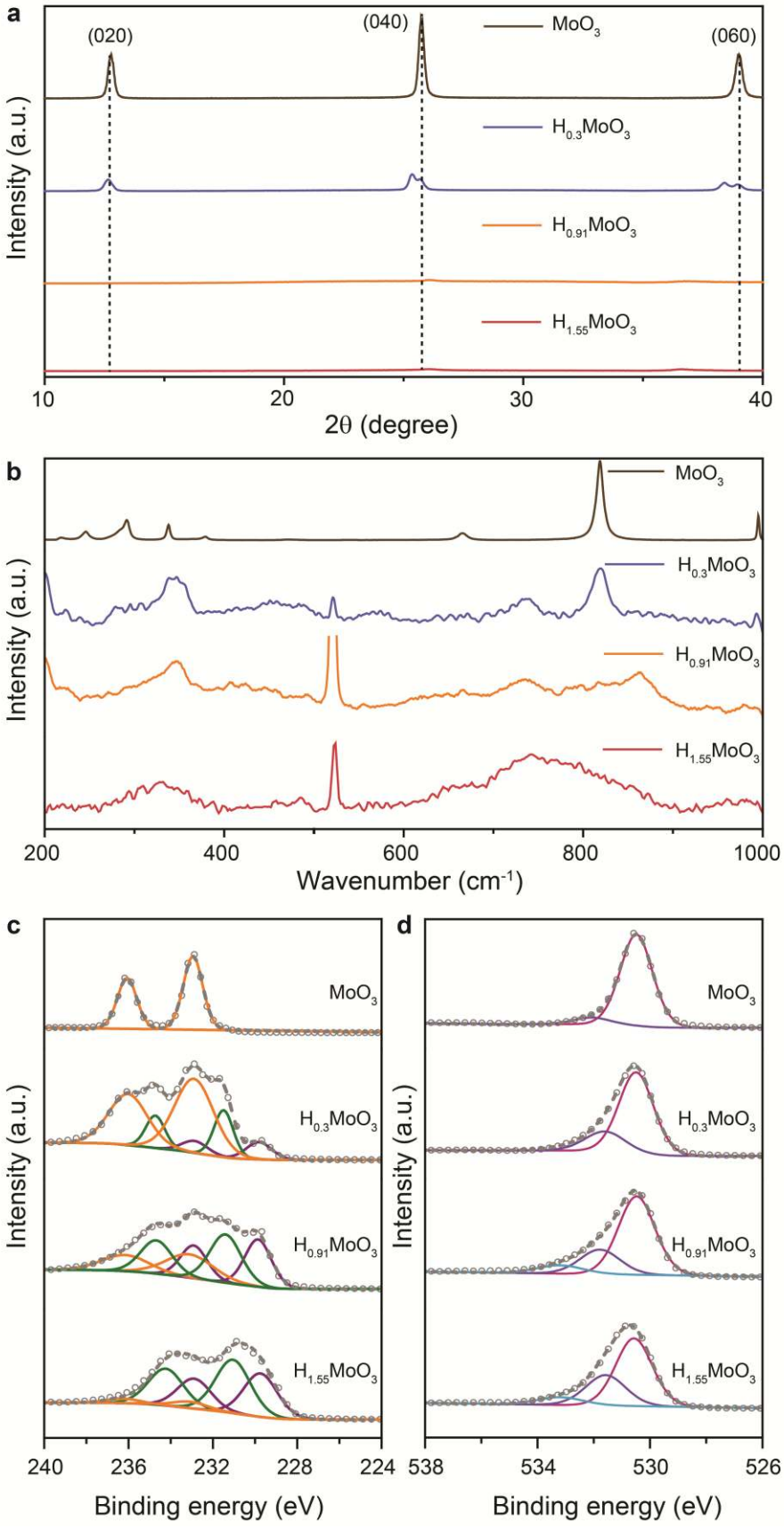

Figure 3. (a) XRD patterns, (b) Raman spectra (peak at 520 cm^{-1} due to the silicon substrate), (c) XPS Mo 3d spectra and (d) XPS O 1s spectra of MoO_3 and the three types of H_xMoO_3 samples.

In order to investigate the electron band structures of the three H_xMoO_3 samples and to compare them with MoO_3, XPS valence spectrum analysis is carried out for determining the valence band position, while photoelectron spectroscopy in air (PESA) is applied for revealing the Fermi level. In **Figure 4**a, for MoO_3, the valence band edge is found to be ~3 eV away from the Fermi level.[33] In comparison, a weak hump is observed between the valence band edge and the Fermi level for slightly intercalated $H_{0.3}MoO_3$. This weak peak corresponds to the overlap of the electron wave functions associated with the occupation of the Mo *4d* states by the free electron introduced from the intercalated H^+.[26, 34] It also indicates that there is a slight semiconductor-to-metal transition.[5d] A closer inspection of the spectra reveals the hump is composed of two small peaks, located at ~0.9 and ~1.9 eV binding energies, in which the 0.9 eV peak (d_1) represent the Mo *4d* band singly filling originated from Mo^{5+} and the ~1.9 eV peak (d_2) results from the doubly occupied Mo^{4+} cations.[34-35] By increasing the amount of intercalated H^+, both the intensities of d_1 and d_2 peaks enhance, suggesting that the samples lose their semiconducting properties and become more metallic.[5d] Interestingly, for $H_{1.55}MoO_3$, the d_2 peak becomes much larger than d_1, suggesting the contribution of Mo^{4+} cations dominates the electronic band structure of highly intercalated H_xMoO_3.

Analysis of the Fermi level values determined by the PESA spectra reveals that there is also a trend of the Fermi level shifting higher with an increasing amount of *x* (Figure 4b and **Figure S7**). Assuming *x* intercalated H^+ introduce *x* free electron into MoO_3, the free electron concentration, based on the

free gas model, is increased from 5.82 × 10^{21} cm^{-3} for slightly intercalated $H_{0.3}MoO_3$ to 3.01 × 10^{22} cm^{-3} for heavily intercalated $H_{1.55}MoO_3$ (**Table S2**), which is believed to be the main cause for the alteration of the Fermi level position.[26]

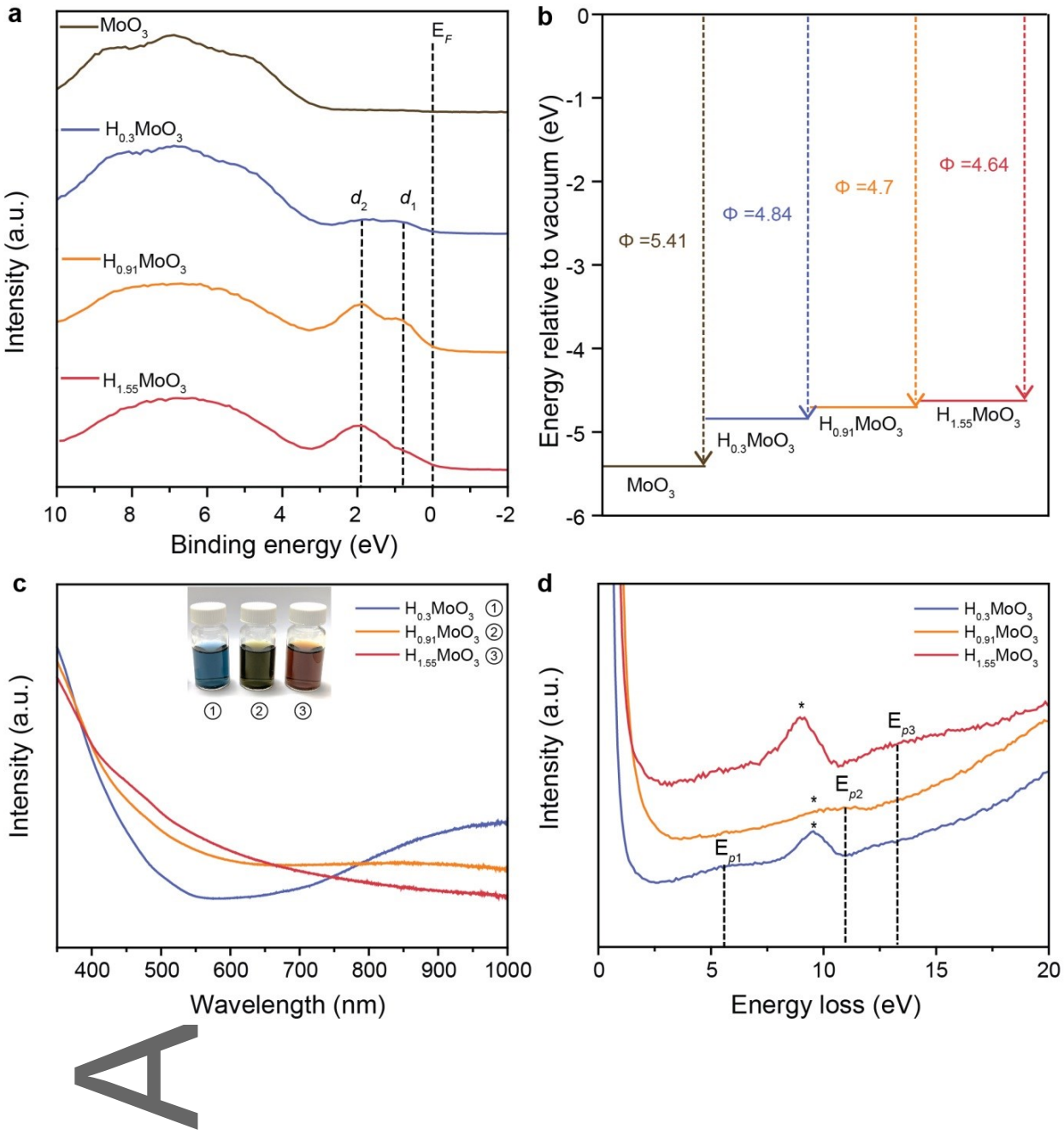

Figure 4. (a) XPS valence spectra and (b) Fermi level positions of MoO_3 in comparison to the three types of H_xMoO_3. (c) UV-Vis-NIR absorption spectra of all three types of H_xMoO_3. The inset shows the original color of $H_{0.3}MoO_3$, $H_{0.91}MoO_3$ and $H_{1.55}MoO_3$ samples as labelled, respectively. (d) EELS spectra of all three types of H_xMoO_3. The peaks marked with "*" are ascribed to the carbon grid background in accordance with EELS spectrum of MoO_3 (Figure S9).

The concurrently injected electrons introduced during the formation of H_xMoO_3 are confirmed to have Drude-like behavior.[7b] Therefore, the significant free electron concentrations in 2D H_xMoO_3 are believed to induce a plasmon resonance in the visible light region. The optical images in the inset of Figure 4c show that $H_{0.3}MoO_3$, $H_{0.91}MoO_3$ and $H_{1.55}MoO_3$ have blue, green and red colors, respectively. The corresponding UV-Vis-NIR absorption spectra of the three H_xMoO_3 samples are shown in Figure 4c. For $H_{0.3}MoO_3$, an obvious absorption peak appears at around 950 nm. By comparing with theoretical calculations using the Mie-Gans theory, this peak can be ascribed to the surface plasmonic peak for the thickness axis (**Supporting Information Note S2** and **Table S3**). For $H_{0.9}MoO_3$, there is an obvious peak at 840 nm and a broad absorption peak hidden on the shoulder between ~450 and ~600 nm. By de-convoluting the absorption spectrum, this peak is identified at 510 nm from **Figure S8**. The position of these two peaks are close to the calculated values of 518 (thickness axis) and 824 nm (lateral dimension axis) according to Table S3. When the sample is transformed to $H_{1.55}MoO_3$, both surface plasmon resonance peaks are further blue-shifted and merged into a broad shoulder. The de-convoluted peak positions are at 425 and 650 nm (Figure S8), which are similar to those of calculated results (435 nm for thickness axis and 660 nm for lateral dimension axis) based on Table S3.

The existence of plasmon resonances in H_xMoO_3 are also confirmed by electron energy loss spectroscopy (EELS), with the EELS spectrum of MoO_3 used as a reference for comparison. In **Figure S9**, the peaks at 6.8 and 9.2 eV can be attributed to the carbon grid background. No obvious energy loss peak ascribed to the free electron induced plasmon is observed, which is consistent with those reported in the literature.[33, 36] For all types of H_xMoO_3 samples (Figure 4d), additional broad peaks can be identified at ~6 (E_{p1}), ~11.3 (E_{p2}) and 13.6 eV (E_{p3}) for $H_{0.33}MoO_3$, $H_{0.91}MoO_3$ and $H_{1.55}MoO_3$, respectively. These values match well with the calculated bulk plasmon energies, which can be assigned to the plasmon mode originated by the free electrons introduced by H^+ intercalation. Detailed calculation and comparison are shown in **Table S4**.

Plasmon resonances in H_xMoO_3 are successfully demonstrated over a wide spectral range, from ~400 nm in the visible light to the near-red end of NIR region as a function of intercalated H^+, which is particularly useful in probing biochemical reactions. This wide optical range allows for the possibility of choosing an optimal operating wavelength to achieve the best performance for plasmonic sensors, specifically in revealing biological redox events. Here, we explore such a capability by developing plasmonic enzymatic glucose sensors based on three types of 2D H_xMoO_3 nanodisks (x = 0.3, 0.91 and 1.55) together with glucose oxidase (GOx). H_xMoO_3 are known to be a class of strongly reducing compounds,[12] which can be highly sensitive to H_2O_2 generated by the oxidation of glucose in the presence of GOx.[37] Here the amount and location of intercalated H^+ ions in various types of H_xMoO_3 are hypothesized to have a great influence on the plasmonic response to H_2O_2 due to the strong H^+ dependence of the system.

To test the hypothesis, glucose in a concentration range of 0.5 μM to 50 mM is added to GOx-H_xMoO_3 solutions (x = 0.3, 0.91 and 1.55). As can be seen by the naked eye (inset in **Figure 5**a, c and

e), it is found that the solution colors of all types of H_xMoO_3 gradually fade with an increase in the exposed glucose concentration, which is associated with the modulation of the corresponding UV-Vis-NIR spectra (Figure 5a, c and e), confirming the interaction between H_xMoO_3 and H_2O_2.

By closely investigating the plasmonic peak of $H_{0.3}MoO_3$, it can be seen that the initial response ratio of the 950 nm absorbance is ~0.1 at 0.5 μM glucose (Figure 5b) with reference to no glucose exposure. This response ratio does not change until the exposed glucose concentration reaches 5 μM. In the range between 5 μM and 0.5 mM, the response ratio increases from ~0.1 to ~0.6. However, above 0.5 mM, the response ratio seems to saturate. For $H_{0.91}MoO_3$ (Figure 5d), the linear response window is greatly improved for both fitted plasmonic peaks of 510 and 840 nm in the region between 5 μM and 50 mM, although the response ratios do not alter when the glucose concentration is reduced to under 5 μM. In the case of $H_{1.55}MoO_3$, the linear response range of both fitted plasmonic peaks at 425 and 650 nm is further extended to the whole range of glucose concentrations with a better response resolution (Figure 5f). The corresponding linear response slopes of $H_{1.55}MoO_3$ for 425 and 650 nm are ~0.3 and ~0.27, respectively, which are significantly larger than those of 510 (~0.22) and 840 nm (~0.15) in $H_{0.91}MoO_3$.

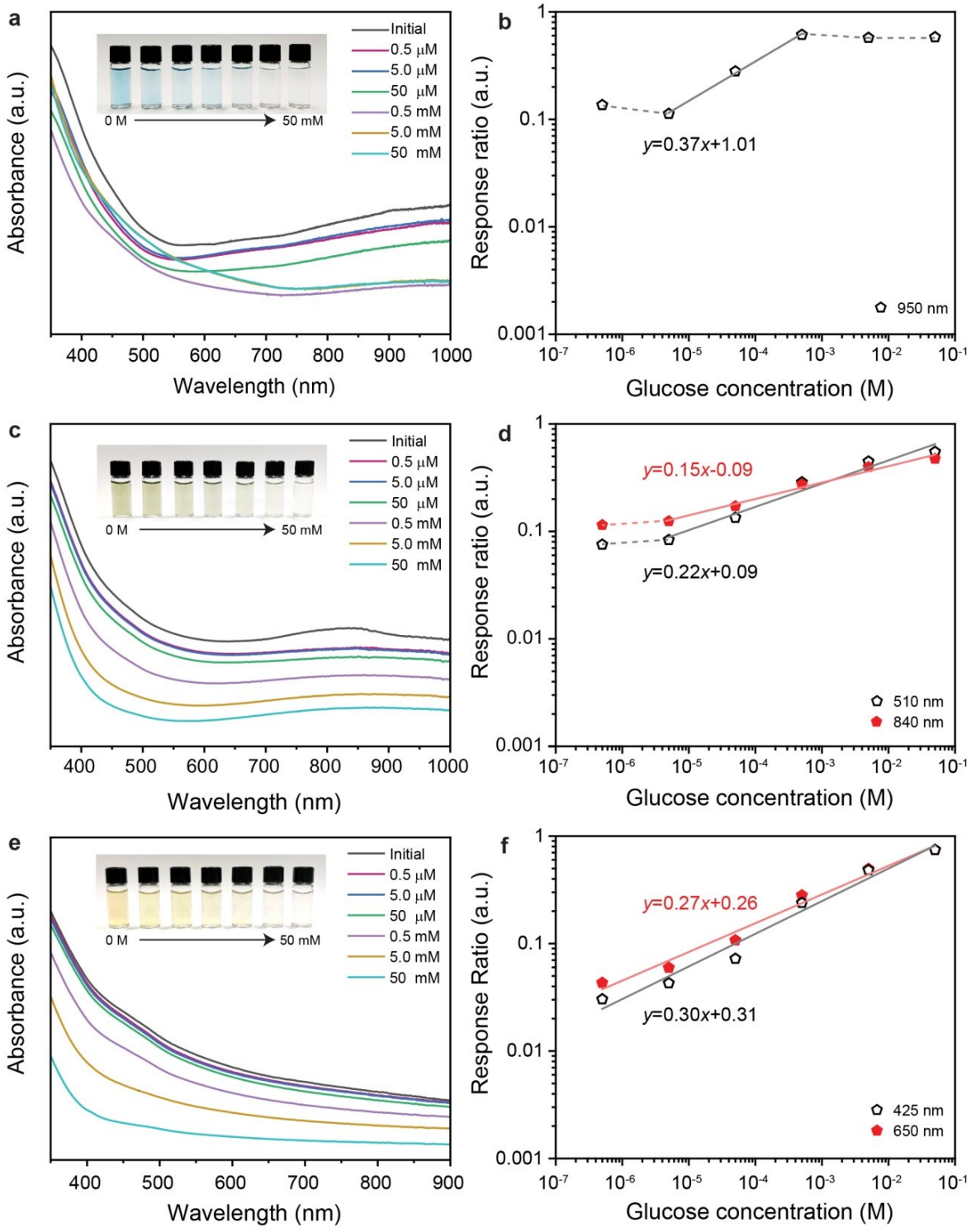

Figure 5. UV-Vis-NIR absorption spectra of (a) $H_{0.3}MoO_3$ (c) $H_{0.91}MoO_3$ and (e) $H_{1.55}MoO_3$ mixed with GOx after the addition of different concentrations of glucose. The insets show the corresponding optical images of H_xMoO_3-GOx suspensions. The response ratio of (b) $H_{0.3}MoO_3$ at 950 nm, (d) $H_{0.91}MoO_3$ at 510 nm and 840 nm, and (f) $H_{1.55}MoO_3$ at 425 nm and 650 nm as a function of the glucose concentration. The response ratio is calculated using $\left|\frac{I_{after}-I_{initial}}{I_{initial}}\right|$, in which $I_{initial}$ and I_{after} are the absorbance before and after the addition of glucose, respectively. The linear region of the response ratio *vs.* glucose concentration is fitted using a solid line, while the saturate region is connected using a dashed line.

To investigate the operating mechanism of the developed plasmonic glucose sensors, Raman spectroscopy and XPS measurements are performed on the 2D H_xMoO_3-GOx samples after exposure to 50 mM glucose (**Figure S10** and **S11**). From Figure S10, for $H_{0.3}MoO_3$, Raman peaks located at ~880, ~940 and ~950 cm^{-1} are attributable to amorphous hydrated molybdenum oxide.[38] For $H_{0.91}MoO_3$ and $H_{1.55}MoO_3$, the Raman peak at 950 cm^{-1} almost vanishes and the intensity of the peak at ~880 cm^{-1} is enhanced, both indicating that the water content in the hydrated compound is significantly increased.[38] In addition, the formation of hydrated molybdenum oxide after the interaction of H_xMoO_3-GOx and glucose can be further verified by the XPS spectra shown in Figure S11, in which the Mo^{6+} oxidation states dominate all three sample spectra. Therefore, based on the evidence provided by the UV-Vis-NIR, Raman and XPS spectra, the glucose sensing mechanism of H_xMoO_3 can be proposed as follows:

H_2O_2, generated from glucose in the presence of GOx, is dissociated into hydroxyl radical (OH·) on the surface of H_xMoO_3.[12] The highly reactive OH· radicals then cleave the OH or OH_2 bonds and remove the H atoms from the exposed terminal O atom site in H_xMoO_3 (**Figure 6**a), forming water molecules which mostly remain in the crystal structure. For $H_{0.3}MoO_3$, a significant number of intercalated H^+ ions form OH groups with the asymmetric coordinated oxygen atoms in MoO_3.[9a, 9c] However, the generated OH· radicals do not favorably react with the H atoms in the intralayer sites due to their relatively higher bonding energies as compared to those in the van der Waals gap,[9c] which therefore explains the early saturation of the absorbance response when the glucose concentration exceeds 0.5 mM (Figure 5b). For both $H_{0.91}MoO_3$ and $H_{1.55}MoO_3$, the concentration of terminal OH or OH_2 groups are significantly increased, which allows the reaction with more generated OH· radicals. This can be the main reason for the extension of the linear response range beyond 0.5 mM glucose. It is also noticed that the lower detection limits for both $H_{0.3}MoO_3$ and $H_{0.91}MoO_3$ are only down to 5 µM, which is much higher than that of $H_{1.55}MoO_3$. This can be possibly due to the limited diffusion of a small amount of generated OH· radicals into the van der Waals gap of both $H_{0.3}MoO_3$ and $H_{0.91}MoO_3$, while this is not applicable to $H_{1.55}MoO_3$ as it is mainly consisted of monolayers.

UV-Vis-NIR spectroscopy cannot be practically integrated into the 2D H_xMoO_3-GOx based plasmonic glucose-sensing system due to its bulky size and relatively high cost. To show that the measurement can be easily adopted into a hand-held electronic circuit configuration, we develop a simple and low-cost LED-photodetector setup to measure the plasmonic glucose-sensing response of H_xMoO_3-GOx in real time (Figure 6b). As the glucose response behaviors differ greatly between $H_{1.55}MoO_3$ and $H_{0.3}MoO_3$, based on the UV-Vis-NIR absorption measurements (Figure 5), commercial LEDs with

operating wavelengths of 410 and 940 nm are selected for $H_{1.55}MoO_3$ and $H_{0.3}MoO_3$, respectively. Our hand-held device consists of an array of LEDs, photodetectors that cover the operating wavelength, and a microcontroller (see the section of "Experimental Details").

As can be observed in Figure 6c and d, upon the addition of glucose both response trends for $H_{0.3}MoO_3$ and $H_{1.55}MoO_3$ are nearly consistent with those measured by UV-Vis-NIR spectroscopy, and the response ratio of $H_{1.55}MoO_3$ is almost triple than that of $H_{0.3}MoO_3$ for all concentrations of glucose solutions. The detection limit of $H_{1.55}MoO_3$ at 410 nm is calculated to be as low as 2 nM based on conventional 3σ theory[37a, 37b, 39], while it is 5 μM for $H_{0.3}MoO_3$ at 940 nm (Figure 6e). Figure 6f shows the response time of both $H_{1.55}MoO_3$ and $H_{0.3}MoO_3$ toward glucose. Both samples demonstrate response times longer with the higher concentrations of glucose solutions, which may be possibly ascribed to the concentration dependency of glucose oxidation kinetics in the presence of GOx. For $H_{1.55}MoO_3$ at 410 nm, the reaction is finished within 10 s for the highest glucose concentration (50 mM). In comparison, the response time for $H_{0.3}MoO_3$ at 940 nm is reduced to 3 s, which can be ascribed to its limited number of reaction sites with OH· radicals according to the sensing mechanism described in the previous section. From **Table S5**, the detection limit of our developed 2D $H_{1.55}MoO_3$-GOx plasmonic sensor is superior to many glucose-sensing systems which are based on noble-metal plasmonics, fluorescence and electrochemistry. In addition, the response time of this sensor is within 10 s, which exceeds the commercial standard[40] and most of the optical glucose sensors (Table S5). It is also within the top range of those based on the electrochemical sensing platform (Table S5).

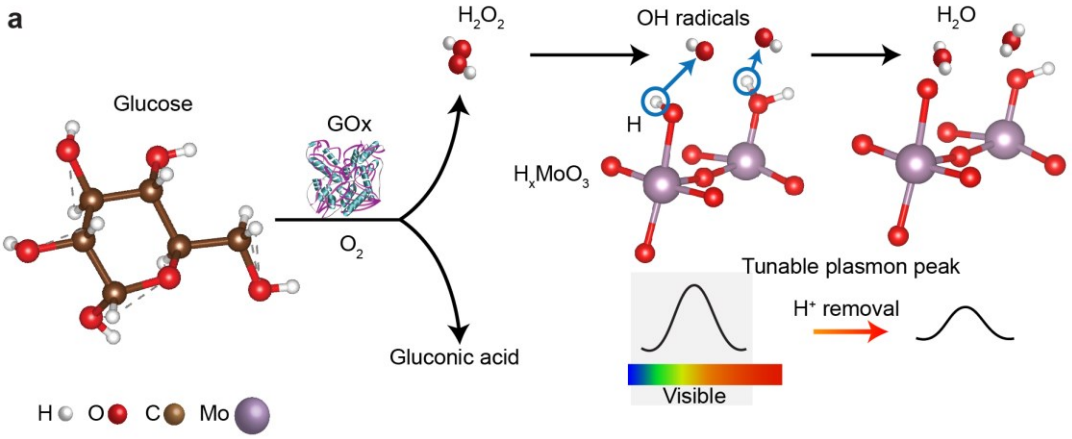
a
Glucose
GOx
O_2
H_2O_2
Gluconic acid
OH radicals
H
H_xMoO_3
H_2O
Tunable plasmon peak
H^+ removal
Visible
H O C Mo

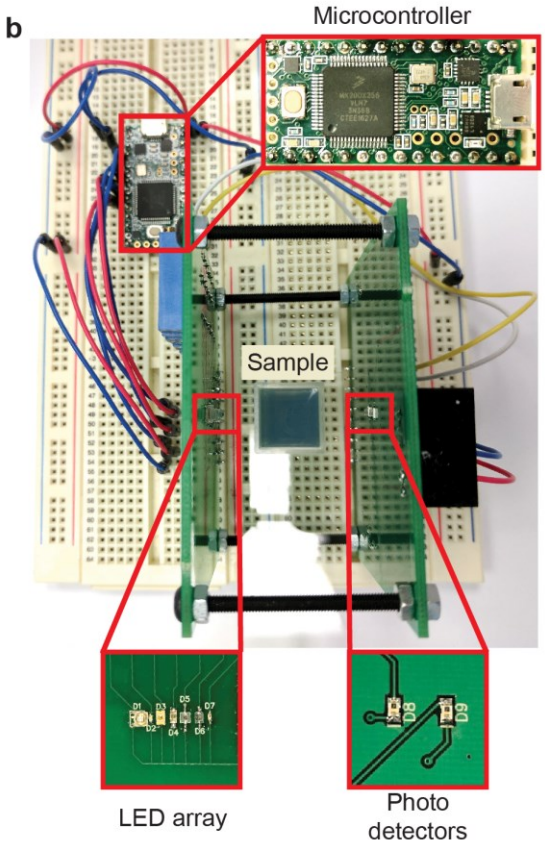
b
Microcontroller
Sample
LED array
Photo detectors

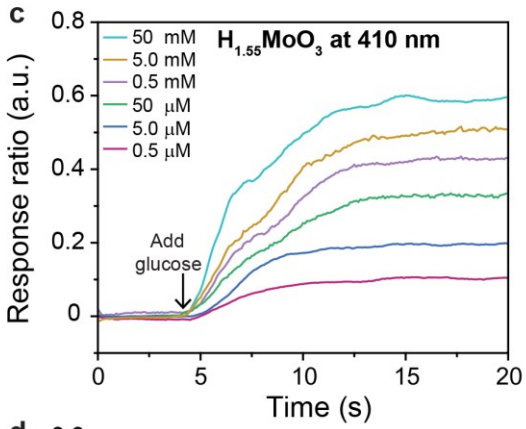
c
50 mM
5.0 mM
0.5 mM
50 μM
5.0 μM
0.5 μM
$H_{1.55}MoO_3$ at 410 nm
Add glucose
Response ratio (a.u.)
Time (s)

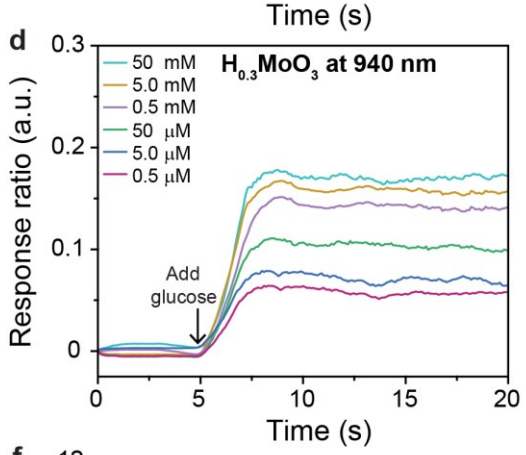
d
50 mM
5.0 mM
0.5 mM
50 μM
5.0 μM
0.5 μM
$H_{0.3}MoO_3$ at 940 nm
Add glucose
Response ratio (a.u.)
Time (s)

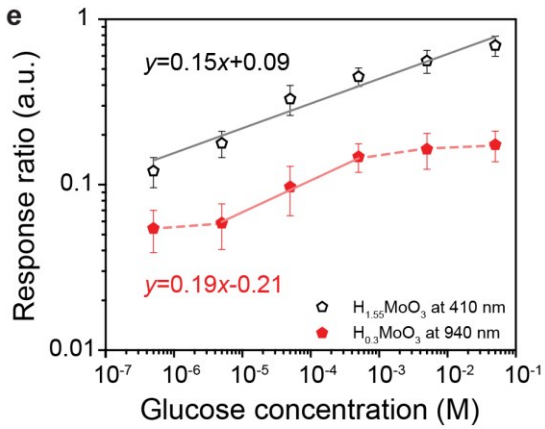
e
y=0.15x+0.09
y=0.19x-0.21
$H_{1.55}MoO_3$ at 410 nm
$H_{0.3}MoO_3$ at 940 nm
Response ratio (a.u.)
Glucose concentration (M)

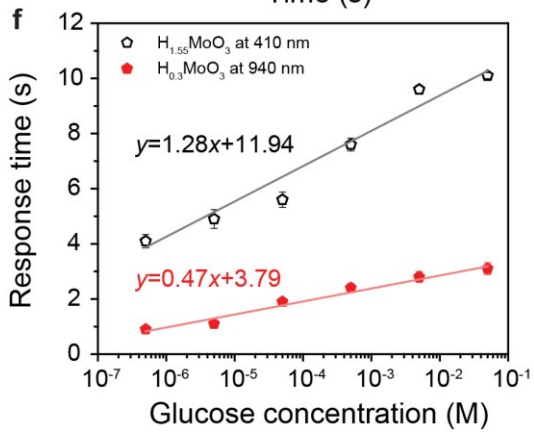
f
$H_{1.55}MoO_3$ at 410 nm
$H_{0.3}MoO_3$ at 940 nm
y=1.28x+11.94
y=0.47x+3.79
Response time (s)
Glucose concentration (M)

Figure 6. (a) The illustration of the glucose sensing mechanism of H_xMoO_3-GOx. (b) The optical image of the LED-photodetector setup. The real-time response of (c) $H_{1.55}MoO_3$ at 410 nm and (d) $H_{0.33}MoO_3$ at 940 nm after the addition of different concentrations of glucose. The corresponding response ratios (e) and time (f) as a function of glucose concentrations of 5 different samples for each type of H_xMoO_3. The response ratio is calculated using $\left|\frac{V_{after}-V_{initial}}{V_{initial}}\right|$, in which $V_{initial}$ and V_{after} are the output voltages from the photodetector in reference to the blank sodium acetate solution before and after the addition of glucose, respectively. The linear region of the response ratio *vs.* glucose concentration is fitted using a solid line, while the saturate region is connected using a dashed line. The sensor response time is defined as the time required for a 90% change in the full magnitude change of the response ratio.

3. Conclusion

In summary, we demonstrated the tunable plasmonics of 2D molybdenum oxides nanodisks driven by H^+ dopants and for the first time explored their application to ultra-sensitive biosensing with fast kinetics. By developing a facile hydrothermal approach for inserting H^+ ions, the intercalation phase and morphology of H_xMoO_3 could be precisely controlled, which had considerable advantages over the conventional Zn/HCl chemical reduction and hydrogen spill-over approaches. An increase in the intercalated H^+ content resulted in a higher degree of exfoliation for the MoO_3 host structure and eventually produced 2D planar nanodisk structures with monolayer thickness when x = 1.55, with a corresponding gradual decrease in crystallinity. At the same time, the Mo oxidation state was reduced from 6+ to a mixture of 5+ and 4+, causing single and double filling of the Mo *4d* state,

respectively, and therefore leading to a semiconductor-to-metal transition. The concurrently injected electrons in H_xMoO_3 were mostly delocalised and led to an increase in the Fermi level. More importantly, these Drude-model-like free electrons produced plasmon resonances in H_xMoO_3 across the whole visible light range and part of the NIR region, which could be readily tuned by the intercalated H^+ concentration.

Through a representative model of enzymatic glucose sensing, we qualitatively and quantitatively demonstrated the ability to use degenerately hydrogen doped plasmonics for the rapid detection of H_2O_2 which was a by-product of the enzymatic oxidation of glucose. Interestingly, the response ratio and linearity were determined by both the H^+ concentration and also the ionic intercalated location in the host crystal structure. It was found that $H_{1.55}MoO_3$, which was a highly H^+ intercalated compound, had the optimum response given by its maximum number of H^+ bonded with the O atoms compared to other phases of H_xMoO_3.

We designed a hand-held LED-photodetector setup for practical implementation of the degenerately H^+ doped plasmonic biosensing concept. The sensor based on $H_{1.55}MoO_3$-GOx showed a detection limit of 2 nM for glucose at 410 nm with the response time within 10 s, which exceeded all reported plasmonic as well as many electrochemical and optical glucose sensors involving enzymatic oxidation. Such an extraordinary performance presents a great opportunity for utilising degenerately hydrogen doped plasmonics in ultra-sensitive probing of biochemical events, breaking the trade-off between operating wavelength, sensitivity and kinetics that currently exists in tunable plasmonic biosensing systems. These features, coupled with the low-cost of the system, lead our plasmonic biosensor to demonstrate a strong commercial potential.

4. Experimental Section

Synthesis of α-MoO_3 nanobelt and 2D H_xMoO_3 nanodisks

Materials were made by dissolving 0.2 mM ammonium molybdate tetrahydrate ($(NH_4)_6Mo_7O_{24}\cdot 4H_2O$, ≥99.9%, Sigma-Aldrich) and 0.8 mM L-(+)-tartaric acid ($C_4H_6O_6$, ≥99.5%, Sigma-Aldrich) in 15 mL distilled water under magnetic stirring at room temperature. The solutions were divided into four portions equally and their pH values were adjusted by the addition of nitric acid (HNO_3, 70%, Sigma Aldrich) to 1, 1.5, 2 and 2.5. The solutions were then transferred into Teflon-lined stainless steel autoclaves and maintained in the oven at 180°C for 5 h. After the hydrothermal synthesis, the samples were carefully washed with distilled water and dried in an N_2 environment naturally.

Structural and morphological characterization

Solid-state ^{1}H MAS NMR experiments were carried out using a Bruker Avance III 500 MHz (11.7 T) spectrometer and a 2.5 mm HX MAS NMR probe. The samples were finely ground, packed into zirconia rotors and spun at 25 kHz. The ^{1}H π/2 pulse length was 2 μs and the chemical shift scale was referenced using TMS. TGA was carried out using a Perkin-Elmer Pyris 1 instrument in N_2 over a temperature range of 30 to 270°C with a heating rate of 10 °C min^{-1}. AFM images were collected using a Bruker Dimension Icon AFM with scan-assist software. The low and high resolution TEM measurements were conducted using JEOL 1010 and JEOL 2100F instruments with a 100 keV and 80 keV acceleration voltage, respectively. EELS was performed using a Gatan Imaging Filter (GIF) Tridium Spectrometer in the JEOL 2100F instrument. XRD patterns were obtained through the Bruker D8 microdiffractometer equipped with a 0.5 mm collimator and a Vantec 500 detector. The

experiment was conducted using a copper source with a potential of 40 kV and a current of 40 mA. Raman spectra were collected using a Horiba Scientific LabRAM HR evolution Raman spectrometer. The samples were excited with a 4.5 mW, 532 nm laser and the measurements were conducted using a 50× lens and 1800 lines per mm grating. XPS was performed using the Thermo Scientific K-alpha system. The samples were scanned under an Al k-α monochromated X-ray source with a passing energy of 50 keV and a duel time of 50 ms. PESA spectra were collected using a Riken Keiki Model AC-2 PESA spectrometer with the probe light energy set to 50 nW and a power law of 1/3. UV-Vis-NIR spectroscopy was carried out using a Cary 500 spectrometer.

Glucose sensing setup

The synthesized H_xMoO_3 dry powder was dispersed in a sodium acetate ($\geq$99%, Sigma-Aldrich) solution at a concentration of 10 µg mL^{-1}. The GOx powder (*from Aspergillus niger*, Type II, Sigma-Aldrich) was also dissolved in the sodium acetate solution at a concentration of 10 mg mL^{-1}. The pH of the sodium acetate solution was adjusted to ~5.2 using a 1 M HCl solution (37%, Sigma Aldrich). The H_xMoO_3-GOx samples were prepared by mixing H_xMoO_3 and GOx at a volume ratio of 5:1 and incubated for 5 min. The glucose solutions of different concentrations were prepared by dissolving the D-(+)-glucose ($\geq$99.5%, Sigma-Aldrich) into sodium acetate solution (pH = ~5.2) with saturated O_2. For investigating the plasmonic properties of H_xMoO_3-GOx with glucose, the H_xMoO_3-GOx was mixed with the glucose solution at a volume ratio of 1:1. Their optical properties were then measured using a UV-Vis-NIR spectroscopy (Cary 500 spectrometer) and a LED-photodetector setup.

For fabricating the LED-photodetector setup, a surface mount InGaN/SiC LED (Bivar Inc., ~1 mW) and a surface mount GaAs LED (Kingbright, ~1 mW) were used as the 410 and 940 nm light sources,

respectively. Silicon photodiodes (Luna Optoelectronics, detection wavelength: 300 – 1100 nm, maximum responsivity: ~0.5 A/W) were used as the photodetector unit. The distance between the LED lamps and the photodetectors was fixed by spacers (Figure 6b). The output voltage from the photodetector was measured every 0.1 s and subsequently amplified and digitalized through a 32 bit microcontroller (K20 Teensy 3.2 Kinetis). The data was then transferred to a computer through a USB cable for real-time display and storage.

Supporting Information

Supporting Information is available from the Wiley Online Library or from the author.

Acknowledgements

The authors would like to acknowledge the fund received from the Australian Research Council (DE160100715). The authors also acknowledge the MNRF and RMMF facilities for providing access to equipment and resources.

Received: ((will be filled in by the editorial staff))
Revised: ((will be filled in by the editorial staff))
Published online: ((will be filled in by the editorial staff))

5. References

[1] a) R. W. Johns, H. A. Bechtel, E. L. Runnerstrom, A. Agrawal, S. D. Lounis, D. J. Milliron, *Nat. Commun* **2016**, 7, 11583; b) J. M. Luther, P. K. Jain, T. Ewers, A. P. Alivisatos, *Nat. Mater.* **2011**, 10, 361; c) P. Guo, R. D. Schaller, J. B. Ketterson, R. P. H. Chang, *Nat. Photon* **2016**, 10,

267; d) A. Kristensen, J. K. W. Yang, S. I. Bozhevolnyi, S. Link, P. Nordlander, N. J. Halas, N. A. Mortensen, *Nat. Rev. Mater.* **2016**, 2, 16088.

[2] a) H. Matsui, Y. L. Ho, T. Kanki, H. Tanaka, J. J. Delaunay, H. Tabata, *Adv. Opt. Mater.* **2015**, 3, 1759; b) X. Wang, Y. Ke, H. Pan, K. Ma, Q. Xiao, D. Yin, G. Wu, M. T. Swihart, *ACS Catal.* **2015**, 5, 2534; c) H. Matsui, S. Furuta, T. Hasebe, H. Tabata, *ACS Appl. Mater. Interfaces* **2016**, 8, 11749.

[3] a) I. Kriegel, F. Scotognella, L. Manna, *Phys. Rep.* **2017**, 674, 1; b) P. K. Jain, K. Manthiram, J. H. Engel, S. L. White, J. A. Faucheaux, A. P. Alivisatos, *Angew. Chem. Int. Ed.* **2013**, 52, 13671; c) R. J. Mendelsberg, P. M. McBride, J. T. Duong, M. J. Bailey, A. Llordes, D. J. Milliron, B. A. Helms, *Adv. Opt. Mater.* **2015**, 3, 1293.

[4] a) M. Kanehara, H. Koike, T. Yoshinaga, T. Teranishi, *J. Am. Chem. Soc.* **2009**, 131, 17736; b) E. Della Gaspera, A. S. Chesman, J. van Embden, J. J. Jasieniak, *ACS Nano* **2014**, 8, 9154.

[5] a) Q. Guo, Y. Yao, Z.-C. Luo, Z. Qin, G. Xie, M. Liu, J. Kang, S. Zhang, G. Bi, X. Liu, J. Qiu, *ACS Nano* **2016**, 10, 9463; b) R. Alam, M. Labine, C. J. Karwacki, P. V. Kamat, *ACS Nano* **2016**, 10, 2880; c) K. Manthiram, A. P. Alivisatos, *J. Am. Chem. Soc.* **2012**, 134, 3995; d) M. M. Alsaif, K. Latham, M. R. Field, D. D. Yao, N. V. Medehkar, G. A. Beane, R. B. Kaner, S. P. Russo, J. Z. Ou, K. Kalantar-zadeh, *Adv. Mater.* **2014**, 26, 3931; e) K. Kalantar-zadeh, J. Z. Ou, T. Daeneke, A. Mitchell, T. Sasaki, M. S. Fuhrer, *Appl. Mater. Today* **2016**, 5, 73.

[6] a) W. Liu, Q. Xu, W. Cui, C. Zhu, Y. Qi, *Angew. Chem. Int. Ed.* **2017**, 56, 1600; b) S. Zhuiykov, L. Hyde, Z. Hai, M. K. Akbari, E. Kats, C. Detavernier, C. Xue, H. Xu, *Appl. Mater. Today* **2017**, 6, 44.

[7] a) X. K. Hu, Y. T. Qian, Z. Song, J. R. Huang, R. Cao, J. Q. Xiao, *Chem. Mater.* **2008**, 20, 1527; b) H. Cheng, M. Wen, X. Ma, Y. Kuwahara, K. Mori, Y. Dai, B. Huang, H. Yamashita, *J. Am. Chem. Soc.* **2016**, 138, 9316.

[8] N. Sotani, K. Eda, M. Sadamatu, S. Takagi, *Bull. Chem. Soc. Jpn.* **1989**, 62, 903.

[9] a) S. Adams, *J. Solid State Chem.* **2000**, 149, 75; b) B. Braïda, S. Adams, E. Canadell, *Chem. Mater.* **2005**, 17, 5957; c) X. Sha, L. Chen, A. C. Cooper, G. P. Pez, H. Cheng, *J. Phys. Chem. C* **2009**, 113, 11399.

[10] K. Schuh, W. Kleist, M. Høj, A. D. Jensen, P. Beato, G. R. Patzke, J.-D. Grunwaldt, *J. Solid State Chem.* **2015**, 228, 42.

[11] H. Negishi, S. Negishi, Y. Kuroiwa, N. Sato, S. Aoyagi, *Phys. Rev. B, PRB* **2004**, 69, 064111.

[12] E. B. Kadossov, A. R. Soufiani, A. W. Apblett, N. F. Materer, *RSC Adv.* **2015**, 5, 97755.

[13] J. Z. Ou, J. L. Campbell, D. Yao, W. Wlodarski, K. Kalantar-Zadeh, *J. Phys. Chem. C* **2011**, 115, 10757.

[14] a) Z.-C. Ma, L.-M. Wang, D.-Q. Chu, H.-M. Sun, A.-X. Wang, *RSC Adv.* **2015**, 5, 27398; b) A. Chithambararaj, N. Sanjini, A. C. Bose, S. Velmathi, *Catal. Sci. Tech.* **2013**, 3, 1405.

[15] Y. Li, J. Cheng, Y. Liu, P. Liu, W. Cao, T. He, R. Chen, Z. Tang, *J. Phys. Chem. C* **2017**, 121, 5208.

[16] a) R. H. Busey, O. L. Keller Jr, *J. Chem. Phys.* **1964**, 41, 215; b) J. Aveston, E. W. Anacker, J. S. Johnson, *Inorg. Chem.* **1964**, 3, 735; c) P. C. H. Mitchell, in *Ullmann's encyclopedia of industrial chemistry*, John Wiley and Sons, Inc., 1990, 675

[17] V. Mastikhin, A. Nosov, V. Terskikh, K. Zamaraev, I. E. Wachs, *J. Phys. Chem.* **1994**, 98, 13621.

[18] C. Ritter, W. Müller‐Warmuth, R. Schöllhorn, *J. Chem. Phys.* **1985**, 83, 6130.

[19] N. Sotani, M. Kunitomo, M. Hasegawa, *Chem. Lett.* **1983**, 12, 647.

[20] a) Q. Mahmood, W. S. Kim, H. S. Park, *Nanoscale* **2012**, 4, 7855; b) Y. Muraoka, J. C. Grenier, S. Petit, M. Pouchard, *Solid State Sci.* **1999**, 1, 133.

[21] H.-S. Kim, J. B. Cook, H. Lin, J. S. Ko, S. H. Tolbert, V. Ozolins, B. Dunn, *Nat. Mater.* **2017**, 16, 454.

[22] K. Kalantar-Zadeh, J. Tang, M. Wang, K. L. Wang, A. Shailos, K. Galatsis, R. Kojima, V. Strong, A. Lech, W. Wlodarski, R. B. Kaner, *Nanoscale* **2010**, 2, 429.

[23] X. W. Lou, H. C. Zeng, *J. Am. Chem. Soc.* **2003**, 125, 2697.

[24] Y. Wang, J. Z. Ou, A. F. Chrimes, B. J. Carey, T. Daeneke, M. M. Y. A. Alsaif, M. Mortazavi, S. Zhuiykov, N. Medhekar, M. Bhaskaran, J. R. Friend, M. S. Strano, K. Kalantar-Zadeh, *Nano Lett.* **2015**, 15, 883.

[25] G.-A. Nazri, C. Julien, *Solid State Ion.* **1992**, 53, 376.

[26] M. M. Alsaif, A. F. Chrimes, T. Daeneke, S. Balendhran, D. O. Bellisario, Y. Son, M. R. Field, W. Zhang, H. Nili, E. P. Nguyen, K. Latham, J. van Embden, M. S. Strano, J. Z. Ou, K. Kalantar-zadeh, *Adv. Funct. Mater.* **2016**, 26, 91.

[27] C. Liu, Z. Li, Z. Zhang, *Appl. Phys. Lett.* **2011**, 99, 223104.

[28] a) K. Eda, *J. Solid State Chem.* **1992**, 98, 350; b) T. Hirata, K. Ishioka, M. Kitajima, *Appl. Phys. Lett.* **1996**, 68, 458.

[29] J. Miciukiewicz, T. Mang, H. Knözinger, *Appl. Catal. A* **1995**, 122, 151.

[30] N. Mohamad Latiff, L. Wang, C. C. Mayorga-Martinez, Z. Sofer, A. C. Fisher, M. Pumera, *Nanoscale* **2016**, 8, 16752.

[31] a) H. Zhang, Y. Wang, E. R. Fachini, C. R. Cabrera, *Electrochem. Solid State Lett.* **1999**, 2, 437; b) T. Barbara, G. Gammie, J. W. Lyding, J. Jonas, *J. Solid State Chem.* **1988**, 75, 183.

[32] A. M. Douvas, M. Vasilopoulou, D. G. Georgiadou, A. Soultati, D. Davazoglou, N. Vourdas, K. P. Giannakopoulos, A. G. Kontos, S. Kennou, P. Argitis, *J. Mater. Chem. C* **2014**, 2, 6290.

[33] M. M. Alsaif, M. R. Field, B. J. Murdoch, T. Daeneke, K. Latham, A. F. Chrimes, A. S. Zoolfakar, S. P. Russo, J. Z. Ou, K. Kalantar-Zadeh, *Nanoscale* **2014**, 6, 12780.

[34] M. T. Greiner, L. Chai, M. G. Helander, W. M. Tang, Z. H. Lu, *Adv. Funct. Mater.* **2012**, 22, 4557.

[35] D. O. Scanlon, G. W. Watson, D. J. Payne, G. R. Atkinson, R. G. Egdell, D. S. L. Law, *J. Phys. Chem. C* **2010**, 114, 4636.

[36] K. Iakoubovskii, K. Mitsuishi, Y. Nakayama, K. Furuya, *Phys. Rev. B* **2008**, 77, 104102.

[37] a) J. Yuan, Y. Cen, X.-J. Kong, S. Wu, C.-L. Liu, R.-Q. Yu, X. Chu, *ACS Appl. Mater. Interfaces* **2015**, 7, 10548; b) L. Jin, L. Shang, S. Guo, Y. Fang, D. Wen, L. Wang, J. Yin, S. Dong, *Biosens. Bioelectron.* **2011**, 26, 1965; c) Y. Xia, J. Ye, K. Tan, J. Wang, G. Yang, *Anal. Chem.* **2013**, 85, 6241; d) W. Tang, L. Li, L. Wu, J. Gong, X. Zeng, *PLoS One* **2014**, 9, e95030.

[38] M. Camacho-López, E. Haro-Poniatowski, L. Lartundo-Rojas, J. Livage, C. Julien, *Mater. Sci. Eng. B* **2006**, 135, 88.

[39] a) H. Ma, X. Liu, X. Wang, X. Li, C. Yang, A. Iqbal, W. Liu, J. Li, W. Qin, *Microchim. Acta* **2017**, 184, 177; b) P.-H. Huang, C. P. Hong, J. F. Zhu, T.-T. Chen, C.-T. Chan, Y.-C. Ko, T.-L. Lin, Z.-B. Pan, N.-K. Sun, Y.-C. Wang, *Dalton Trans.* **2017**, 46, 6985; c) X. W. Shen, C. Z. Huang, Y. F. Li, *Talanta* **2007**, 72, 1432.

[40] H.-C. Wang, A.-R. Lee, *J. Food Drug. Anal.* **2015**, 23, 191.

[41] X. Gu, H. Wang, Z. D. Schultz, J. P. Camden, *Anal. Chem.* **2016**, 88, 7191.

[42] X. Liu, S. Zhang, P. Tan, J. Zhou, Y. Huang, Z. Nie, S. Yao, *Chem. Commun.* **2013**, 49, 1856.

[43] H. He, X. Xu, H. Wu, Y. Jin, *Adv. Mater.* **2012**, 24, 1736.

[44] F. Su, L. Zhang, X. Kong, F. Lee, Y. Tian, D. R. Meldrum, *Sens. Biosensing. Res.* **2017**, 14, 1.

[45] J. Li, Y. Li, S. A. Shahzad, J. Chen, Y. Chen, Y. Wang, M. Yang, C. Yu, *Chem. Commun.* **2015**, 51, 6354.

[46] J. Yuan, W. Guo, E. Wang, *Biosens. Bioelectron.* **2008**, 23, 1567.

[47] G. Yang, K. L. Kampstra, M. R. Abidian, *Adv. Mater.* **2014**, 26, 4954.

[48] S. Palanisamy, S. Cheemalapati, S.-M. Chen, *Mater. Sci. Eng. C.* **2014**, 34, 207.

[49] F. Hu, S. Chen, C. Wang, R. Yuan, Y. Chai, Y. Xiang, C. Wang, *J. Mol. Catal. B: Enzym.* **2011**, 72, 298.

[50] K.-J. Chen, C.-F. Lee, J. Rick, S.-H. Wang, C.-C. Liu, B.-J. Hwang, *Biosens. Bioelectron.* **2012**, 33, 75.

[51] H. Muguruma, Y. Shibayama, Y. Matsui, *Biosens. Bioelectron.* **2008**, 23, 827.

[52] V. Mani, B. Devadas, S.-M. Chen, *Biosens. Bioelectron.* **2013**, 41, 309.

[53] D. Liu, W. Lei, J. Hao, D. Liu, B. Liu, X. Wang, X. Chen, Q. Cui, G. Zou, J. Liu, S. Jiang, *J. Appl. Phys.* **2009**, 105, 023513.

[54] M. M. Alsaif, M. R. Field, T. Daeneke, A. F. Chrimes, W. Zhang, B. J. Carey, K. J. Berean, S. Walia, J. van Embden, B. Zhang, K. Latham, K. Kalantar-zadeh, J. Z. Ou, *ACS Appl. Mater. Interfaces* **2016**, 8, 3482.

[55] S. Balendhran, J. Deng, J. Z. Ou, S. Walia, J. Scott, J. Tang, K. L. Wang, M. R. Field, S. Russo, S. Zhuiykov, *Adv. Mater.* **2013**, 25, 109.

The table of contents figure:

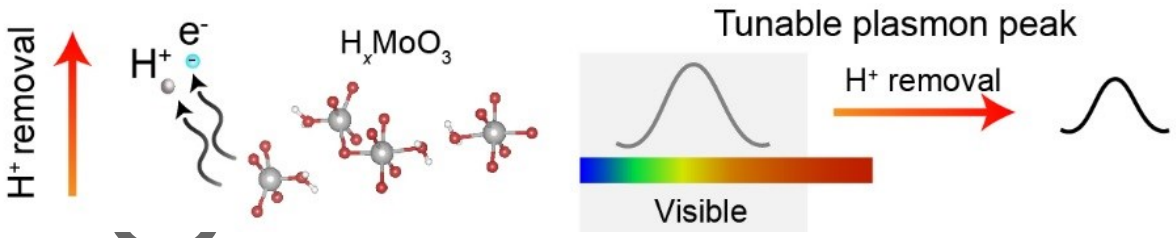

The table of contents entry:

H_xMoO_3 plasmonic disks are sythesised. H^+ and concurrently electrons can be extracted from the host structure during a designed biochemical event. This alteration in charge rapidly changes the plasmon resonance features, hence creating an ultra-sensitive platform.

Supporting Information

Degenerately hydrogen doped molybdenum oxide nanodisks for ultra-sensitive plasmonic biosensing

Bao Yue Zhang, Ali Zavabeti, Adam F. Chrimes, Farjana Haque, Luke A. O'Dell, Hareem Khan, Nitu Syed, Robi Datta, Yichao Wang, Anthony S. R. Chesman, Torben Daeneke, Kourosh Kalantar-zadeh, Jian Zhen Ou**

B. Y. Zhang, A. Zavabeti, Dr. A. F. Chrimes, F. Haque, H. Khan, N. Syed, R. Datta, Dr. T. Daeneke, Prof. K. Kalantar-zadeh, Dr. J. Z. Ou

School of Engineering, RMIT University, Melbourne, VIC 3000, Australia

E-mail: jianzhen.ou@rmit.edu.au and kourosh.kalantar@rmit.edu.au

Dr. A. F. Chrimes

Department of Chemistry and Applied Biosciences, Institute for Chemical and Bioengineering, ETH Zürich, Zürich 8093, Switzerland

Dr. L. A. O'Dell

Institute for Frontier Materials, Deakin University, Geelong, Victoria 3216, Australia

Dr. Y. Wang

School of Life and Environmental Sciences, Deakin University, Geelong, Victoria 3216, Australia

Dr. A. S. R. Chesman

CSIRO Manufacturing, Ian Wark Laboratories, Clayton, Victoria 3168, Australia

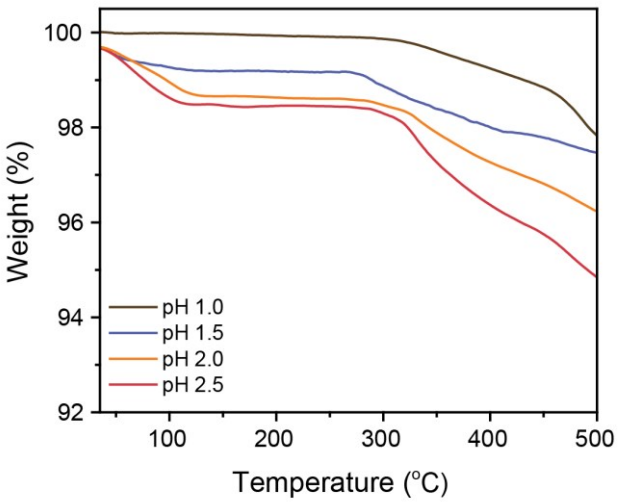

Figure S1. The TGA patterns of samples hydrothermally synthesized at pH 1, 1.5, 2 and 2.5 at temperatures between 30 and 500°C in an N_2 gas environment.

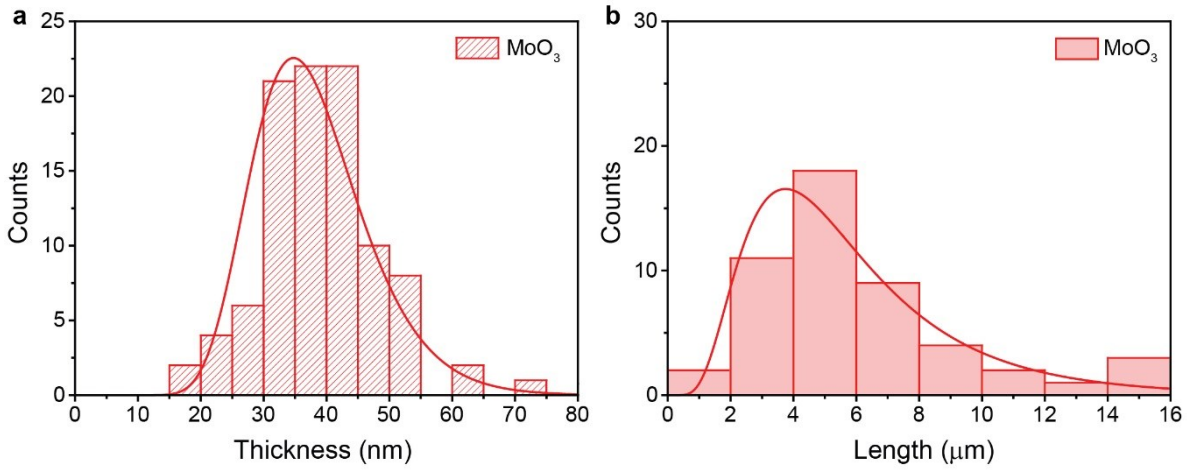

Figure S2. (a) Thickness and (b) length dimension distributions of MoO_3 using 100 samples each. Statistics were extracted from the AFM data.

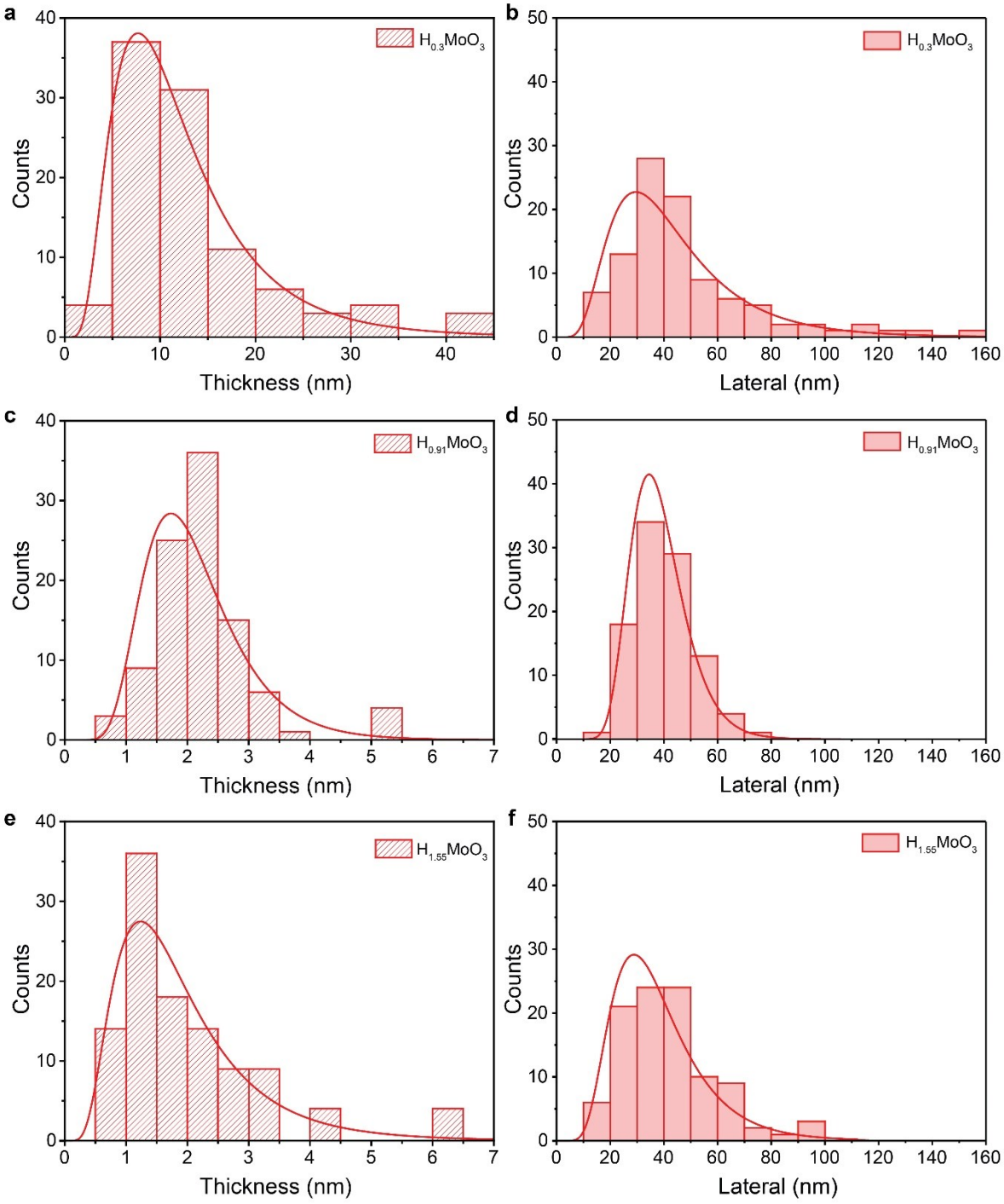

Figure S3. (a) Thickness and (b) lateral distributions of $H_{0.3}MoO_3$. (c) Thickness and (d) lateral distributions of $H_{0.91}MoO_3$. (e) Thickness and (f) lateral distributions of $H_{1.55}MoO_3$. Statistics were extracted from the AFM data and each distribution was obtained from 100 samples.

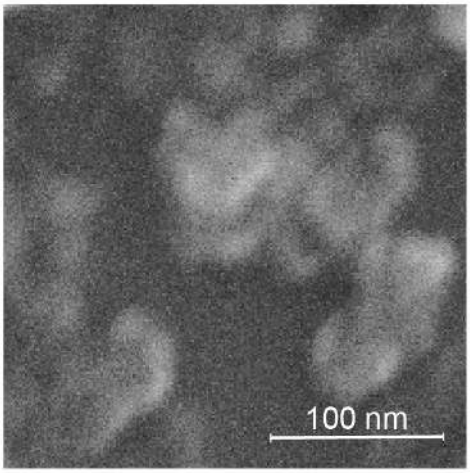

Figure S4. The SEM image of typical H_xMoO_3.

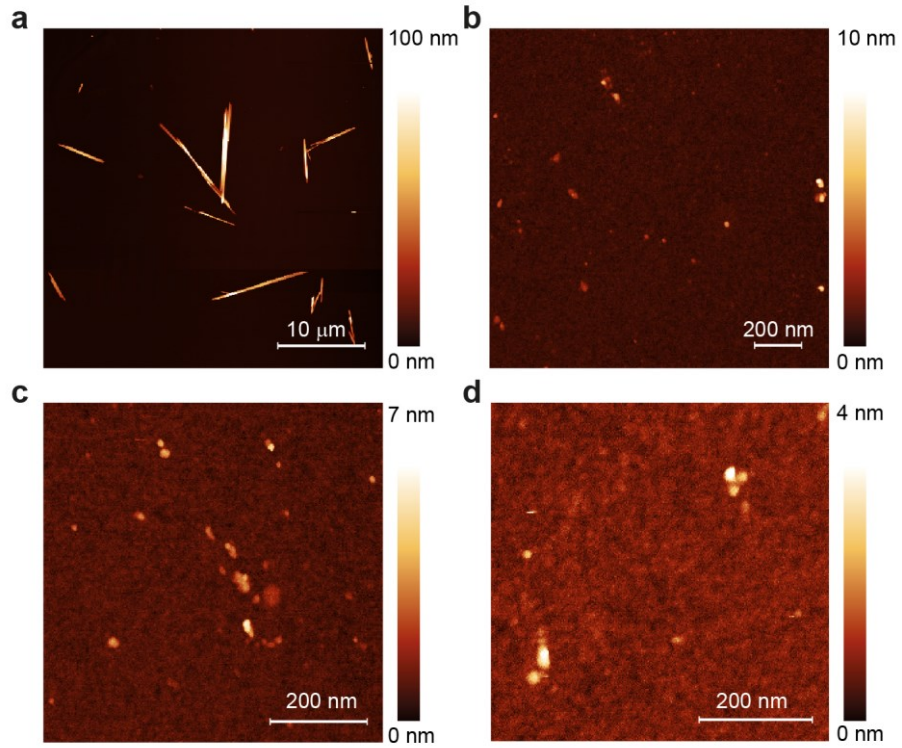

Figure S5. The collective AFM images of (a) α–MoO_3, (b) $H_{0.3}MoO_3$, (c) $H_{0.91}MoO_3$ and (d) $H_{1.55}MoO_3$.

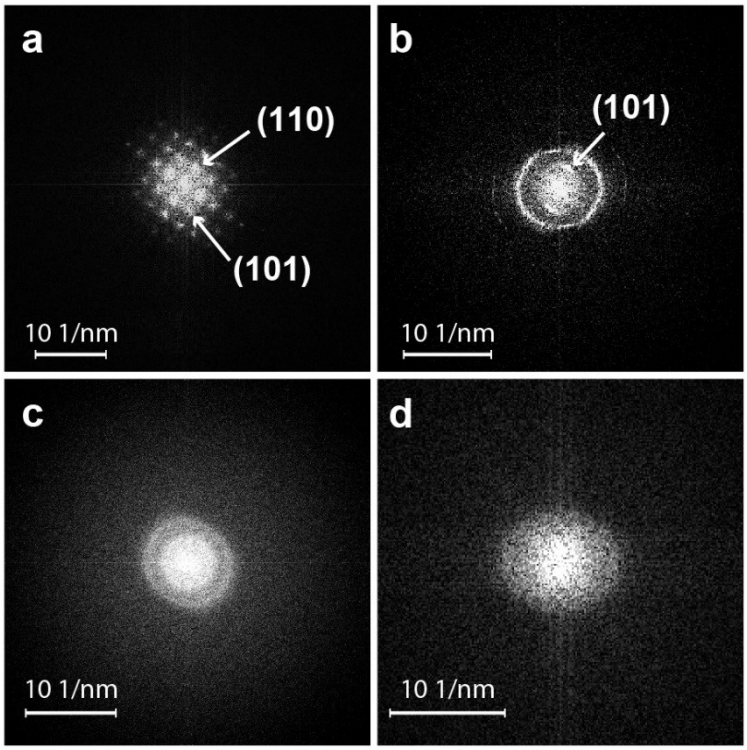

Figure S6. The SEAD patterns of (a) α–MoO_3, (b) $H_{0.3}MoO_3$, (c) $H_{0.91}MoO_3$ and (d) $H_{1.55}MoO_3$.

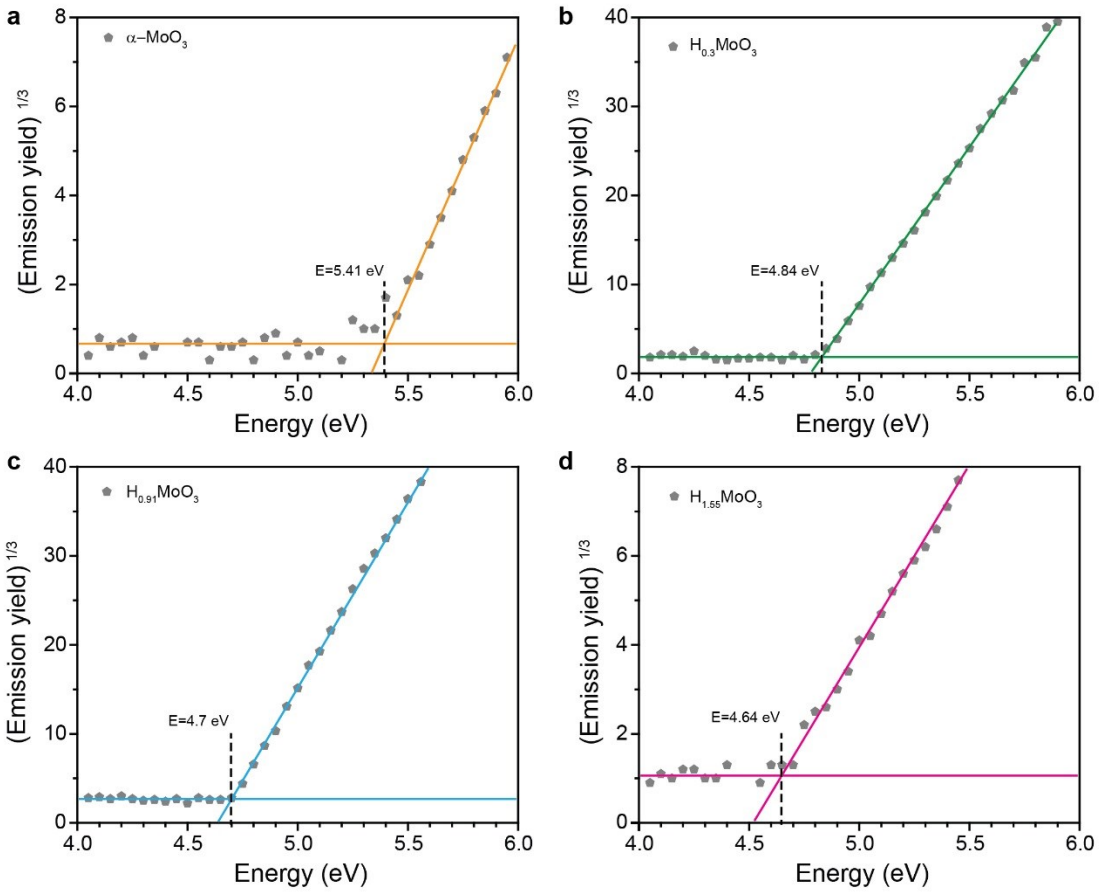

Figure S7. The PESA spectra of (a) α–MoO_3, (b) $H_{0.3}MoO_3$, (c) $H_{0.91}MoO_3$ and (d) $H_{1.55}MoO_3$.

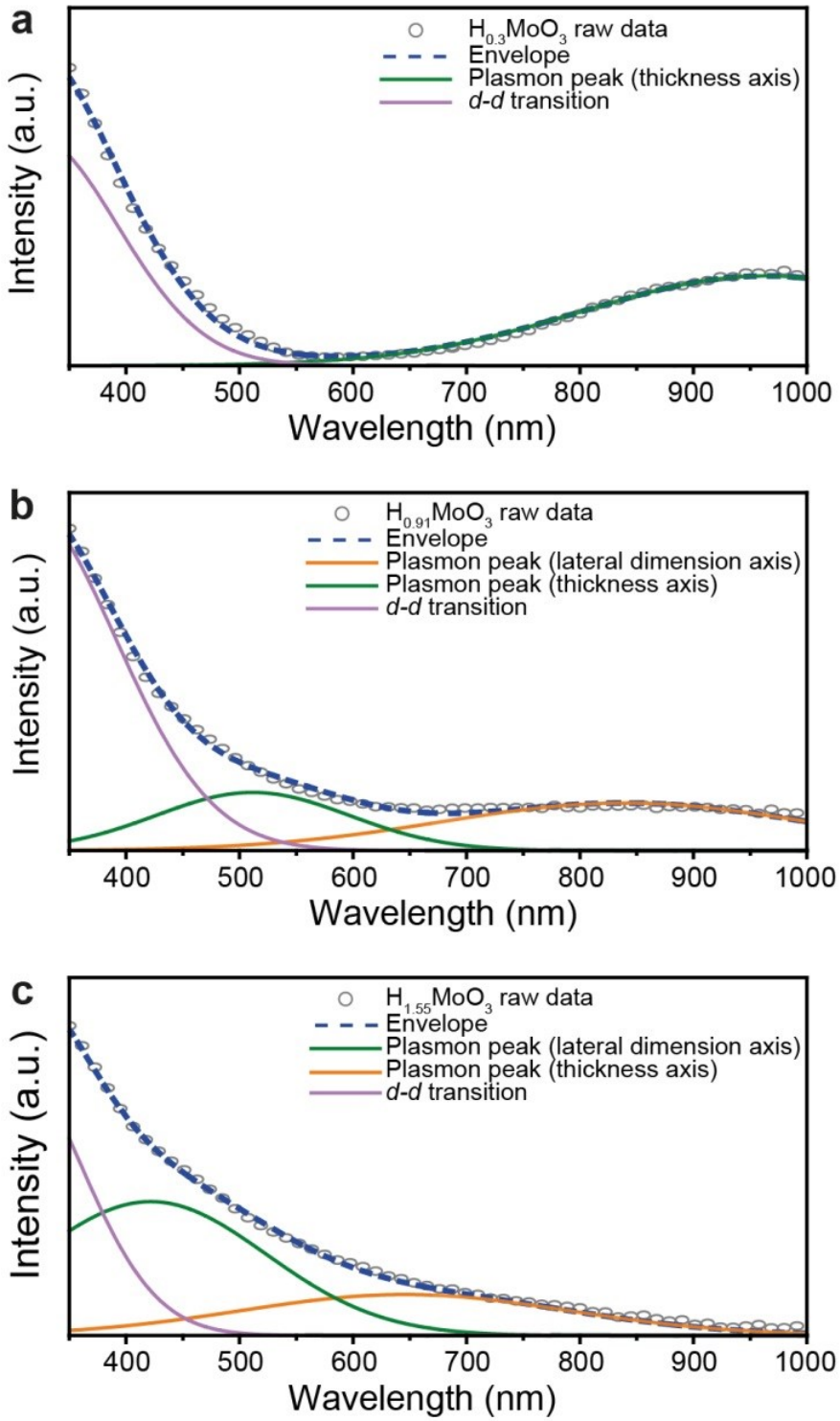

Figure S8. Fitted surface plasmon resonance absorption spectra of (a) $H_{0.3}MoO_3$, (b) $H_{0.91}MoO_3$ and (c) $H_{1.55}MoO_3$.

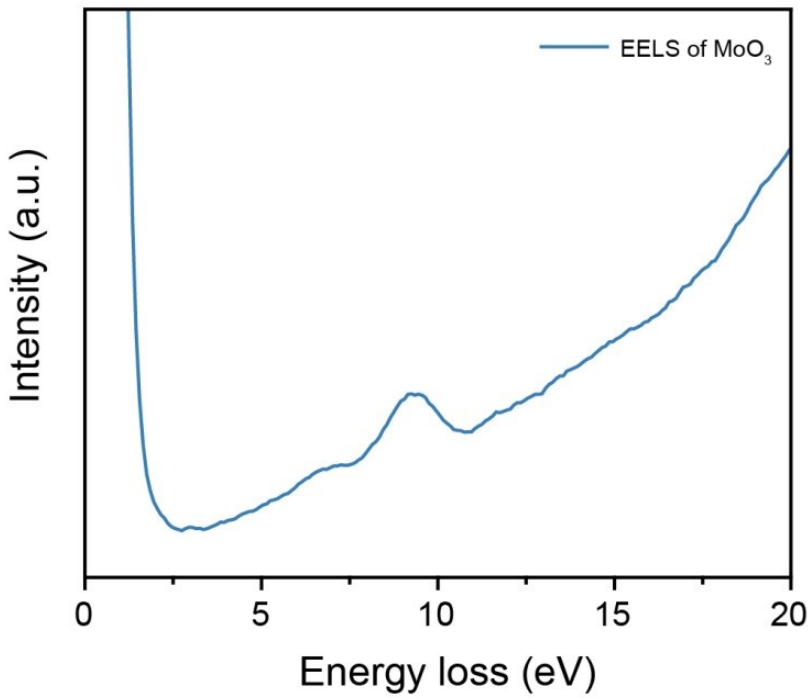

Figure S9. EELS spectrum of α–MoO_3.

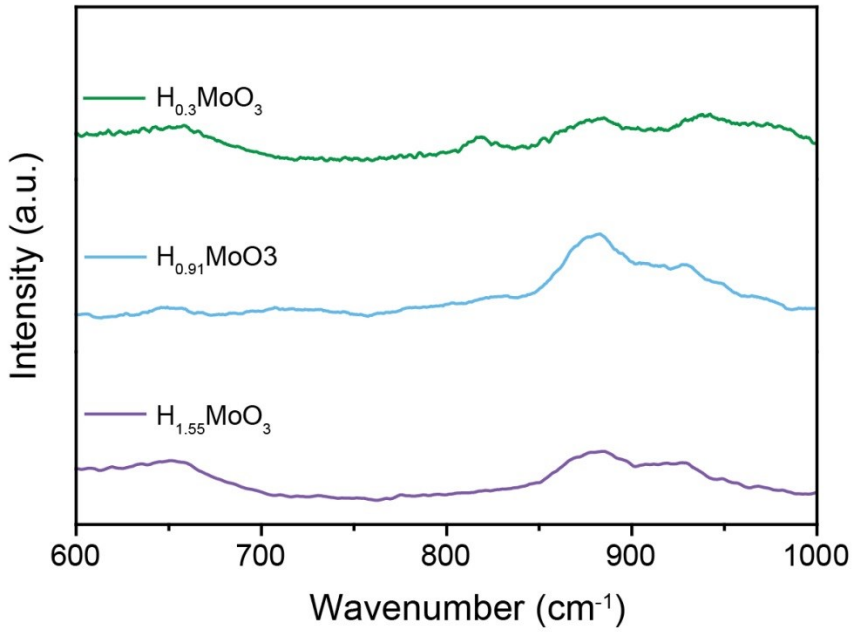

Figure S10. Raman spectra of the three types of H_xMoO_3 after the addition of glucose solution at the concentration of 50 mM.

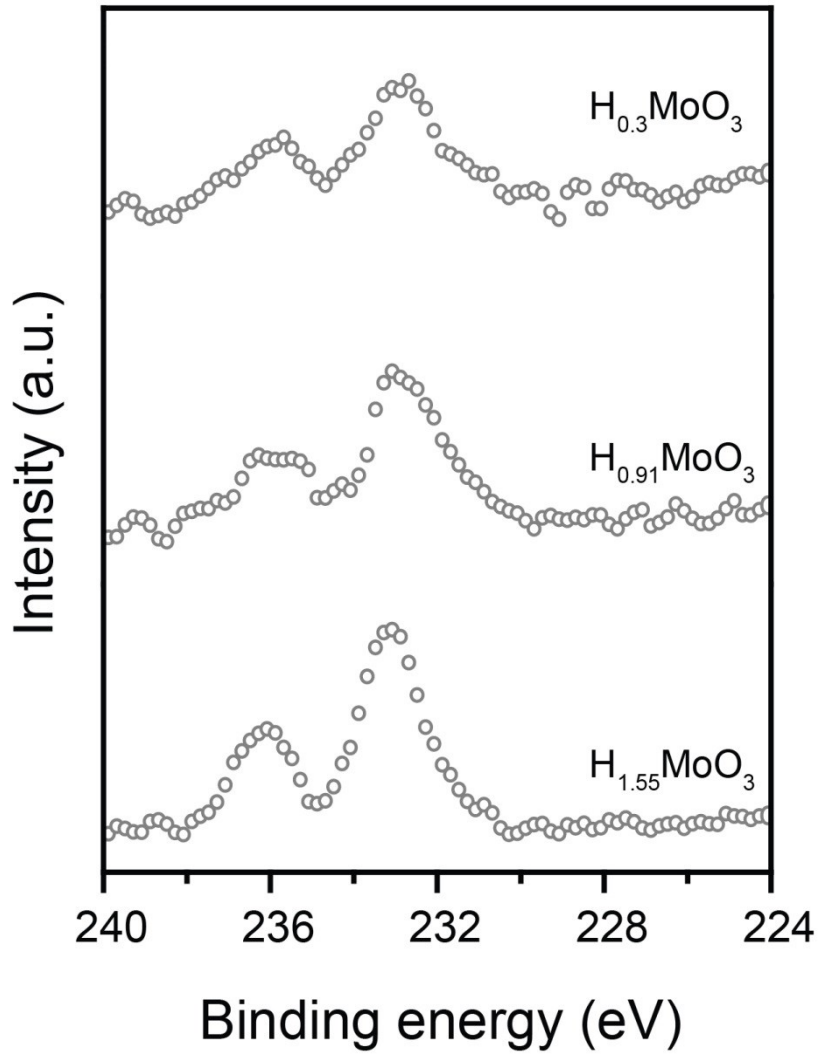

Figure S11. XPS Mo 3d spectra of the three types of H_xMoO_3 after the addition of glucose solution at the concentration of 50 mM.

Table S1. Theoretical calculation of weight loss after the decomposition of H_xMoO_3 to MoO_3

Material	Calculated weight loss (%)	Observed weight loss (%) in this work	Observed weight loss (%) by Sotani *et. al*.[8]
$H_{0.21}MoO_3$	0.15	-	0.4
$H_{0.3}MoO_3$	0.23	0.25	-
$H_{0.91}MoO_3$	0.63	0.79	0.89
$H_{1.55}MoO_3$	1.06	1.01	1.38

Table S2. The theoretical calculated free electron concentrations of three types of H_xMoO_3 assuming each intercalated H^+ bringing one free electron.

Material	Free electron concentration (cm^{-3})
$H_{0.3}MoO_3$	5.82×10^{21}
$H_{0.91}MoO_3$	1.77×10^{22}
$H_{1.55}MoO_3$	3.01×10^{22}

Table S3. Comparison between calculated and measured surface plasmon resonance peaks for all types of H_xMoO_3

Material	Calculation		Observation	
	Thickness axis (nm)	Lateral dimension axis (nm)	Thickness axis (nm)	Lateral dimension axis (nm)
$H_{0.3}MoO_3$	935	1112	950	out of the measurement range
$H_{0.91}MoO_3$	518	824	510	840
$H_{1.55}MoO_3$	435	660	425	650

Table S4. Comparison between calculated and measured bulk plasmon peaks for all types of H_xMoO_3

Material	Calculated bulk plasmon peak (eV)	Observed bulk plasmon peak (eV)
$H_{0.3}MoO_3$	6.3	6
$H_{0.91}MoO_3$	11	11.3
$H_{1.55}MoO_3$	14.4	13.6

Table S5. Comparison of detection limit, response time and measurement range for current enzymatic glucose sensors

Plasmonic glucose sensor				
Materials	**LOD (μM)**	**Response time**	**Measurement range**	**Reference**
2D $H_{1.55}MoO_3$	**0.002**	**<10 s**	**$5 \times 10^{-7} – 5 \times 10^{-2}$ M**	**This work**
Au NPs	<1	20 min	$5 \times 10^{-4} – 5 \times 10^{-3}$ M	[41]
Au NRs	100	2 h	$1 \times 10^{-4} – 1 \times 10^{-3}$ M	[42]
Ag/Au NS	0.5	-	$5 \times 10^{-7} – 2 \times 10^{-5}$ M	[43]
Fluorescent glucose sensor				
Materials	**LOD (μM)**	**Response time**	**Measurement range**	**Reference**
MnO_2- UCNPs	3.7	40 min	$1 \times 10^{-5} – 4 \times 10^{-4}$ M	[37a]
Oxygen sensing film	50	2 min	$5 \times 10^{-5} – 5 \times 10^{-3}$ M	[44]
Ag NPrs	2.5	90 min	$2.5 \times 10^{-6} – 2 \times 10^{-4}$ M	[45]
CdTe QD	0.01	5 min	$1 \times 10^{-6} – 1 \times 10^{-3}$ M	[46]
CDs-MnO_2	0.053	5 min	$3 \times 10^{-5} – 1 \times 10^{-4}$ M	[39a]
Electrochemical glucose sensor				
Materials	**LOD (μM)**	**Response time**	**Measurement range**	**Reference**
MWCNTs/GOx/PTFE/GC	5	<15 s	$2.5 \times 10^{-3} – 4 \times 10^{-2}$ M	[37d]
PEDOT-GOx	120	-	$1 \times 10^{-4} – 5 \times 10^{-3}$ M	[47]
GOx/MWCNT/GO	28	5 s	$5 \times 10^{-5} – 2 \times 10^{-2}$ M	[48]

GOx/ZnO/GOx/MWCNTs/GC	~2	10 s	$1 \times 10^{-3} – 6 \times 10^{-3}$ M	[49]
CS-GA-GOx/Nafion/PtPd-WCNTs/GC	31	5 s	$6.2 \times 10^{-5} – 1.4 \times 10^{-2}$ M	[50]
PPF/GOx/SWCNTs/PPF/Au	6	4 s	$2.5 \times 10^{-5} – 2.2 \times 10^{-3}$ M	[51]
GOx/ Nafion /ERGO-MWCNTs/GC	4.7	5 s	$1 \times 10^{-5} – 6.5 \times 10^{-3}$ M	[52]

NP: nanoparticle, NS: nanoshell, NR: nanorod, NPr: nanoprism, NC: nanocluster, UCNP: pconversion nanoparticle, QD: quantum dot, CD: carbon dot, MWCNT: multiwalled carbon nanotubes, GO: graphene oxide, GOx: glucose oxidase, PEDOT: poly(3,4-ethylenedioxythiophene), PTFE: Polytetrafluoroethylene, GC: glassy carbon electrode, CS: chitosan, GA: glucoamylase, SWCNT: a single-walled carbon nanotube, PPF: plasma-polymerized film, ERGO: electrochemically reduced graphene oxide.

Supporting Information Note S1. Raman peak assignment of MoO_3 samples

The 246 cm^{-1} and 338 cm^{-1} peaks represent the bending mode for single bond wagging with oxygen atoms (Mo–O). The 284 cm^{-1}, 292 cm^{-1} and 379 cm^{-1} peaks correspond to the double bond (Mo=O) vibrations. The 667 cm^{-1} peak is assigned to the triply coordinated oxygen (Mo_3–O) stretching mode, which results from edge-shared oxygen atoms in common to three adjacent octahedral. The strongest peak at 818 cm^{-1} represents the doubly coordinated oxygen (Mo_2–O) stretching mode, which is from the corner-sharing oxygen atoms common to the two octahedra, and 995 cm^{-1} peak is assigned to the terminal oxygen (Mo=O) stretching mode.[5d, 11, 13, 53]

Supporting Information Note S2. Theoretical calculations for plasmon resonance peaks of 2D H_xMoO_3 nanodisks

According to Mie-Gans theory the extinction coefficient is given by:[54]

$$A \propto \omega\varepsilon_m^{\frac{3}{2}} \sum_j \frac{\left[\frac{1}{P_j^2}\right]\varepsilon_2}{\left[\varepsilon_1 + \frac{1-P_j}{P_j}\varepsilon_m\right]^2 + \varepsilon_2^2} \quad \text{(S1)}$$

where ω is the angular frequency of incident light; ε_m is the dielectric constant of the medium, ε_1 and ε_2 are the real and imaginary terms of the dielectric function of the suspended material, respectively and the p_j are the depolarization factors for axes (a, b and c). The depolarization factors for the 2D material are:[54]

$$P_B = \frac{1}{g^2}\left[1 - \left(\frac{1-g^2}{g^2}\right)^{\frac{1}{2}} \sin^{-1} g\right] \quad \text{(S2)}$$

$$P_A = P_C = \frac{1-P_B}{2} \quad \text{(S3)}$$

in which the g factor is:

$$g = \left(\frac{a^2-b^2}{a^2}\right)^{1/2} \quad \text{(S4)}$$

Aspect ratios in the 2D system are defined as the length (a) over thickness (b). The depolarization factors of lateral dimensions are considered to be equal in the 2D system (length (a) = width (c)).[5d]

The dielectric function is described by the Lorentz model as:

$$\varepsilon(\omega) = \varepsilon_1 + i\varepsilon_2 = \varepsilon_\infty - \frac{\omega_p^2}{\omega^2 + i\gamma\omega} \quad \text{(S5)}$$

in which ω_p is the bulk plasma frequency, ε_∞ is the high-frequency relative dielectric constant which is equal to ~ 20.[55] γ is the damping coefficient of the resonance.[5d]

$$\omega_p = \sqrt{\frac{Ne^2}{\varepsilon_0 m_e}} \quad \text{(S6)}$$

where N is the free electron concentration, e is the elementary charge, ε_0 is the permittivity of free space, and m_e is the effective mass of an electron (~0.2 m_o for 2D MoO_x),[55] where $m_o = 9.11 \times 10^{31}$kg.

$$\gamma = \frac{1}{\tau} = \frac{e^2}{\sigma m_e} \quad \text{(S7)}$$

where τ is the scattering time of an electron and σ is the conductivity of the material.

References

[1] N. Sotani, K. Eda, M. Sadamatu, S. Takagi, *Bull. Chem. Soc. Jpn.* **1989**, 62, 903.

[2] X. Gu, H. Wang, Z. D. Schultz, J. P. Camden, *Anal. Chem.* **2016**, 88, 7191.

[3] X. Liu, S. Zhang, P. Tan, J. Zhou, Y. Huang, Z. Nie, S. Yao, *Chem. Commun.* **2013**, 49, 1856.

[4] H. He, X. Xu, H. Wu, Y. Jin, *Adv. Mater.* **2012**, 24, 1736.

[5] J. Yuan, Y. Cen, X.-J. Kong, S. Wu, C.-L. Liu, R.-Q. Yu, X. Chu, *ACS Appl. Mater. Interfaces* **2015**, 7, 10548.

[6] F. Su, L. Zhang, X. Kong, F. Lee, Y. Tian, D. R. Meldrum, *Sens. Biosensing. Res.* **2017**, 14, 1.

[7] J. Li, Y. Li, S. A. Shahzad, J. Chen, Y. Chen, Y. Wang, M. Yang, C. Yu, *Chem. Commun.* **2015**, 51, 6354.

[8] J. Yuan, W. Guo, E. Wang, *Biosens. Bioelectron.* **2008**, 23, 1567.

[9] H. Ma, X. Liu, X. Wang, X. Li, C. Yang, A. Iqbal, W. Liu, J. Li, W. Qin, *Microchim. Acta* **2017**, 184, 177.

[10] W. Tang, L. Li, L. Wu, J. Gong, X. Zeng, *PLoS One* **2014**, 9, e95030.

[11] G. Yang, K. L. Kampstra, M. R. Abidian, *Adv. Mater.* **2014**, 26, 4954.

[12] S. Palanisamy, S. Cheemalapati, S.-M. Chen, *Mater. Sci. Eng. C.* **2014**, 34, 207.

[13] F. Hu, S. Chen, C. Wang, R. Yuan, Y. Chai, Y. Xiang, C. Wang, *J. Mol. Catal. B: Enzym.* **2011**, 72, 298.

[14] K.-J. Chen, C.-F. Lee, J. Rick, S.-H. Wang, C.-C. Liu, B.-J. Hwang, *Biosens. Bioelectron.* **2012**, 33, 75.

[15] H. Muguruma, Y. Shibayama, Y. Matsui, *Biosens. Bioelectron.* **2008**, 23, 827.

[16] V. Mani, B. Devadas, S.-M. Chen, *Biosens. Bioelectron.* **2013**, 41, 309.

[17] a) H. Negishi, S. Negishi, Y. Kuroiwa, N. Sato, S. Aoyagi, *Phys. Rev. B, PRB* **2004**, 69, 064111; b) D. Liu, W. Lei, J. Hao, D. Liu, B. Liu, X. Wang, X. Chen, Q. Cui, G. Zou, J. Liu, S. Jiang, *J. Appl. Phys.* **2009**, 105, 023513; c) M. M. Alsaif, K. Latham, M. R. Field, D. D. Yao, N. V. Medehkar, G. A. Beane, R. B. Kaner, S. P. Russo, J. Z. Ou, K. Kalantar-zadeh, *Adv. Mater.* **2014**, 26, 3931; d) J. Z. Ou, J. L. Campbell, D. Yao, W. Wlodarski, K. Kalantar-Zadeh, *J. Phys. Chem. C* **2011**, 115, 10757.

[18] M. M. Alsaif, M. R. Field, T. Daeneke, A. F. Chrimes, W. Zhang, B. J. Carey, K. J. Berean, S. Walia, J. van Embden, B. Zhang, K. Latham, K. Kalantar-zadeh, J. Z. Ou, *ACS Appl. Mater. Interfaces* **2016**, 8, 3482.

[19] S. Balendhran, J. Deng, J. Z. Ou, S. Walia, J. Scott, J. Tang, K. L. Wang, M. R. Field, S. Russo, S. Zhuiykov, *Adv. Mater.* **2013**, 25, 109.

The table of contents figure:

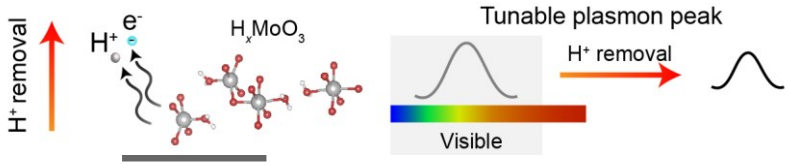

The table of contents entry:

H_xMoO_3 plasmonic disks are sythesised. H^+ and concurrently electrons can be extracted from the host structure during a designed biochemical event. This alteration in charge rapidly changes the plasmon resonance features, hence creating an ultra-sensitive platform.

Author/s:
Zhang, BY;Zavabeti, A;Chrimes, AF;Haque, F;O'Dell, LA;Khan, H;Syed, N;Datta, R;Wang, Y;Chesman, ASR;Daeneke, T;Kalantar-zadeh, K;Ou, JZ

Title:
Degenerately Hydrogen Doped Molybdenum Oxide Nanodisks for Ultrasensitive Plasmonic Biosensing

Date:
2018-03-14

Citation:
Zhang, B. Y., Zavabeti, A., Chrimes, A. F., Haque, F., O'Dell, L. A., Khan, H., Syed, N., Datta, R., Wang, Y., Chesman, A. S. R., Daeneke, T., Kalantar-zadeh, K. & Ou, J. Z. (2018). Degenerately Hydrogen Doped Molybdenum Oxide Nanodisks for Ultrasensitive Plasmonic Biosensing. ADVANCED FUNCTIONAL MATERIALS, 28 (11), https://doi.org/10.1002/adfm.201706006.